Automated snow avalanche release area delineation in data sparse, remote, and forested regions

John Sykes[1], Pascal Haegeli[1], Yves Bühler[2]

[1]Geography Department, Simon Fraser University, Burnaby, British Columbia, Canada
[2]WSL Institute for Snow and Avalanche Research SLF, Davos, Switzerland

Correspondence to: John Sykes (John_Sykes@sfu.edu)

Abstract. Potential avalanche release area (PRA) modelling is critical for generating automated avalanche terrain maps which provide low-cost large scale spatial representations of snow avalanche hazard for both infrastructure planning and recreational applications. Current methods are not applicable in mountainous terrain where high-resolution elevation models are unavailable and do not include an efficient method to account for avalanche release in forested terrain. This research focuses on expanding an existing PRA model to better incorporate forested terrain using satellite imagery and presents a novel approach for validating the model using local expertise, thereby broadening its application to numerous mountain ranges worldwide. The study area of this research is a remote portion of the Columbia Mountains in southeastern British Columbia, Canada which has no pre-existing high-resolution spatial data sets. Our research documents an open source workflow to generate high-resolution DEM and forest land cover data sets using optical satellite data processing. We validate the PRA model by collecting a polygon dataset of observed potential release areas from local guides, using a method which accounts for the uncertainty of human recollection and variability of avalanche release. The validation dataset allows us to perform a quantitative analysis of the PRA model accuracy and optimize the PRA model input parameters to the snowpack and terrain characteristics of our study area. Compared to the original PRA model our implementation of forested terrain and local optimization improved the percentage of validation polygons accurately modelled by 11.7 percentage points and reduced the number of validation polygons that were underestimated by 14.8 percentage points. Our methods demonstrate substantial improvement in the performance of the PRA model in forested terrain and provide means to generate the requisite input datasets and validation data to apply and evaluate the PRA model in vastly more mountainous regions worldwide than was previously possible.

1 Introduction

Snow avalanches are a significant natural hazard for traffic and settlement infrastructure as well as for individuals who travel in snow covered mountainous regions. Roads, railroads, utilities, and permanent structures that are located in areas with potential avalanche hazard can be destroyed by large avalanche impacts or blocked for extended periods during winter storm

28 events causing financial losses and potential for injury or death from individuals being buried in the debris. In economically

29 developed countries, the majority of avalanche fatalities occur during recreational activities (i.e., backcountry skiing,

30 snowmobile riding, mountaineering) where individuals voluntarily expose themselves to avalanche hazard (Boyd et al., 2009),

31 and accident avalanches are mostly triggered by the party that is caught (Schweizer and Lütschg, 2001; Techel et al., 2016).

32 In North America and Europe, an average of approximately 140 people are killed in avalanches each year (Jamieson et al.,

33 2010; Techel et al., 2016; Colorado Avalanche Information Center, 2020).

34 To mitigate avalanche hazard, locations with potential for avalanche release need to be identified so elements at risk can

35 attempt to minimize their exposure by avoiding those areas, minimizing their exposure time, or implementing avalanche

36 control methods (McClung and Schaerer, 2006). Avalanche hazard mapping is a time honored practice for determining the

37 spatial distribution of snow avalanche hazards (Margreth and Funk, 1999; Rudolf-Miklau et al., 2015). Traditional manual

38 hazard mapping combines multiple methods such as terrain inspection, numerical simulations, avalanche event databases and

39 personal experience to evaluate avalanche hazard exposure and spatial extent making it both labor and cost intensive. This

40 highly detailed approach is the gold standard for determining avalanche zoning for permanent infrastructure, but the costs

41 make it unsuitable for mapping large areas of mountainous terrain (Bühler et al., 2018).

42 To overcome this challenge, automated GIS and remote sensing based methods have been developed to expedite the mapping

43 process and produce avalanche terrain indication maps based on digital elevation model (DEM) and land cover data (Maggioni

44 and Gruber, 2003; Gruber and Haefner, 1995). The foundation of automated avalanche terrain mapping is potential avalanche

45 release area (PRA) modelling, which estimates the location of potential hazards based on the local terrain characteristics

46 (Bühler et al., 2013, 2018; Veitinger et al., 2016). PRA models can be applied to define the spatial extent of release areas in

47 dynamic avalanche simulations, which estimate the runout distance, velocity, and flow height of avalanche debris (Christen et

48 al., 2010), or as a standalone spatial layer to assist with hazard identification and trip planning for recreational activities. Their

49 ability to operate at the mountain range scale with limited human input dramatically reduces cost and time to develop spatial

50 data sets which can assist infrastructure planners and recreationists in making more informed decisions about their avalanche

51 hazard exposure (Bühler et al., 2018a, b).The development of large-scale avalanche hazard indication maps in Switzerland has

52 led to them being applied as a tool to help backcountry recreationists visualize terrain hazards and incorporate them into their

53 trip planning process (Harvey et al., 2018).

54 The current state of the art methods for PRA modelling have been developed and validated in regions with widely available

55 high-resolution DEM and forest cover data as well as long term records of avalanche observations (Bühler et al., 2018;

56 Veitinger et al., 2016). However, the majority of mountainous regions in the world do not have freely available high-resolution

57 DEM or forest cover data yet, and long term spatially accurate records of avalanche release are very rare. This seriously limits

58 the application and local validation of PRA models around the world.

59 An additional limitation of existing high-resolution PRA models (e.g., Bühler et al., 2018; Veitinger et al., 2016) is that they

60 do not account for the interaction between forest characteristics and avalanche release. Both the Bühler 2018 and Veitinger

61 2016 PRA models allow for forested areas to be excluded from PRA calculations based on a forest mask layer, but they do not

62 explicitly capture forest avalanche interaction. This reduces the applicability of these PRA models in mountain ranges where

63 a significant portion of the avalanche terrain is forest covered, such as in western North America.

64 To address these challenges and make PRA models applicable more broadly, the objective of this research is to develop a cost-

65 effective workflow for generating the required input datasets for the Bühler et al. (2018) PRA model using satellite data and

66 open-source remote sensing methods. In addition, we present a relatively simple method for adapting the current PRA model

67 to work in forested terrain. In the absence of long-term avalanche observations, we developed a novel approach for utilizing

68 the expertise and terrain knowledge of local mountain guides to validate the PRA model output and optimize the input

69 parameter for the unique terrain and snowpack characteristics of our study area. These three developments—the use of satellite

70 data, the adaptation of the model to work in forested terrain, and the validation with local terrain expertise—together open new

71 opportunities for applying state of the art avalanche terrain modelling in regions with limited existing datasets and resources.

2 Background

73 Avalanche release area modelling and forest avalanche interaction are both areas of active research which have laid the

74 foundation for our research. This section provides context on the fundamentals and development of these research areas with

75 focus on relevant topics for the development of our research methods.

2.1 Potential Avalanche Release Area Modelling

77 Early versions of GIS based avalanche terrain models (Ghinoi and Chung, 2005; Gruber and Haefner, 1995; Maggioni and

78 Gruber, 2003) struggled to outperform simple slope based avalanche release area estimates (Voellmy, 1955) due to the inability

79 of low resolution DEM (20–30 m) to detect small scale terrain features. Current PRA modelling methods evolved over the

80 course of a decade and benefit from developments in high-resolution DEM production and remote sensing (Andres and Chueca

81 Cía, 2012; Barbolini et al., 2011; Bühler et al., 2013, 2018; Chueca Cía et al., 2014; Pistocchi and Notarnicola, 2013; Veitinger

82 et al., 2016; Kumar et al., 2016, 2019). Bühler et al (2013) found that 5 m DEM resolution is the optimal tradeoff between

83 processing efficiency and small-scale feature identification for PRA modelling. To define avalanche release areas the

84 algorithms use DEM derivatives (i.e., slope angle, terrain ruggedness, curvature, and aspect) which rely on focal functions of

85 DEM pixels. With DEM pixel sizes of 5m, a common nine cell focal neighborhood (3x3) is 225 m^2 which is well below the

86 median slab size for human triggered avalanches of 4,000 m^2 (Schweizer and Lütschg, 2001). Adequate PRA model resolution

87 is essential to capture sub-release area scale terrain characteristics which are critical for accurate modelling of human avalanche

88 triggering.

89 The development of these algorithms depends on a robust data set of observed avalanche events to determine appropriate

90 terrain characteristic thresholds which define avalanche release areas. Such datasets can be created through recording of manual

91   observations or generated by applying satellite mapping (Lato et al., 2012; Bühler et al., 2019; Hafner et al., 2021). The

92   combination of terrain characteristics varies between the different algorithms, but some common parameters are slope angle,

93   curvature, roughness, and aspect. In addition to DEM derived terrain variables many algorithms use vegetation coverage to

94   define PRA based on the assumption that avalanche release is less common in areas with tall and dense vegetation. The addition

95   of vegetation cover to a PRA model requires an additional input dataset, which can be generated from satellite imagery, created

96   from locally available forest inventory datasets, or calculated from existing DEM data.

97   The most comprehensive known avalanche release area validation dataset currently available is curated by the WSL Institute

98   for Snow and Avalanche Research SLF in Davos, Switzerland with experienced staff manually mapping avalanche outlines

99   throughout the winter in the surrounding mountain areas. This avalanche observation catalog began in 1970, and as of 2016 it

100   includes 5785 mapped avalanches (Bühler et al., 2018). This dataset is now expanded including data from satellite avalanche

101   mapping (Bühler et al., 2019) as well as airplane (Bühler et al., 2009; Korzeniowska et al., 2017) and drone surveys (Bühler

102   et al., 2017).

103   Using a subset of this validation dataset, Bühler et al. (2018) compared their PRA algorithm performance against another PRA

104   model (Veitinger et al., 2016) and a simple slope based release area estimation method from Voellmy (1955). The results

105   indicate slightly better performance for the Bühler et al. (2018) PRA model over the Veitinger et al. (2016) PRA model, with

106   lower probability of false detection and higher measures of Pierce skill score and Heidke skill score. An additional advantage

107   of the Bühler et al. (2018) PRA model is the ability to convert the raster based PRA model output to polygon features using

108   object based image analysis. Converting the PRA model output to polygon features enables the PRA model to be paired with

109   dynamic avalanche simulation software (Christen et al., 2010; Bühler et al., 2018a,b) to estimate runout distance, impact

110   pressures, flow depth and velocity of the avalanche flow. This powerful combination of release area and runout modelling

111   represent the state of the art of current avalanche terrain indication modelling practices and are a valuable resource for large

112   scale avalanche hazard indication mapping. Therefore, this research seeks to improve and expand upon the existing Bühler et

113   al. (2018) PRA model.

114   The Bühler et al. (2018) PRA model has been applied in multiple regions worldwide, including Chile, Alaska, Afghanistan,

115   and India. However, the input parameters have not been independently tested and optimized using local validation data.

116   Therefore, it is unknown whether the input parameters optimized for Davos, Switzerland are appropriate for mountain regions

117   with different topographic and snowpack characteristics. Our research aims to address this knowledge gap by applying an

118   updated version of the Bühler et al. (2018) PRA model to the Columbia Mountains of southeast British Columbia, Canada and

119   seeks to optimize the input parameters for the study area based on locally available validation data.

2.2 Avalanches in Forested Terrain

121   Avalanche release in forested terrain is an active research area due to the importance of forests as protective barriers from

122   avalanche runout in alpine communities (Casteller et al., 2018; Feistl et al., 2014) and the complex processes that drive the

123 spatial distribution of forested release areas (Lutz and Birkeland, 2011; Teich et al., 2012; Bebi et al., 2009). The snowpack in

124 forested areas is generally more stable due to the anchoring effect of trees, forest canopy snow interception, the disruption of

125 the continuity of weak layers due to snow drop from canopy, and altered snow surface radiation and temperature conditions.

126 However, it is still possible for avalanches to release in forested areas, especially in areas with steep slope angles, low tree

127 density, or in openings within forested areas (Bebi et al., 2009). Small and medium avalanches generally do not have enough

128 impact force to damage trees or tree stands, and forests tend to reduce their runout potential by detraining snow from the

129 flowing avalanche (Feistl et al., 2014). Larger avalanches can break or uproot trees and cause massive destruction to the forest

130 ecosystem (Feistl et al., 2015; Bebi et al., 2009). The location of avalanche release areas in relation to the forest plays a large

131 role in whether trees will impede avalanche flow or be destroyed and possibly entrained (Teich et al., 2012).

132 The ability to account for forest characteristics in avalanche terrain modelling is largely based on locally available data sets.

133 Laser scanning or LiDAR data provide high-resolution DSM and DTM datasets to characterize the forest character, including

134 canopy height, location and size of forest gaps, and basal area (Brožová et al., 2020; Dash et al., 2016). Vegetation height

135 models derived from DSM and DTM data can be used to identify forests with protective function and input as forest masks in

136 PRA models (Bühler et al., 2018; Waser et al., 2015). Similar to their application for DEM production, the high accuracy of

137 these data sets comes at a high cost. Recently, drone-based photogrammetry became a flexible and economic solution to create

138 a forest height layer in combination with an existing DTM, but this methodology can only generate DSM data and only cover

139 limited areas of a few square kilometers.

140 Alternative lower cost methods for estimating forest characteristics include traditional field based sample plots and radar or

141 optical remote sensing instruments (Hyyppä et al., 2000; Ginzler and Hobi, 2015; Rahimizadeh et al., 2020; Waser et al.,

142 2015). The most accessible of these alternative methods is satellite based optical imagery, which can be used to create a forest

143 land cover classification, to determine the extent of the forested area (Bühler et al., 2013), and can be combined with field plot

144 observations of specific forest characteristics to create a predictive model based on the spectral and textural characteristics of

145 the imagery (Dash et al., 2016; Rahimizadeh et al., 2020).

146 Prior research has attempted to incorporate forest characteristics with PRA modelling (Sharp et al., 2018), but low resolution

147 DEM and forest data combined with a limited validation data set make it challenging to evaluate the overall performance of

148 the model. However, the principle of adjusting the potential for avalanche release based on forest character aligns with

149 analytical and theoretical understanding of avalanche release in forested terrain (Bebi et al., 2009; Teich et al., 2012; McClung,

150 2001). This research aims to expand existing methods for capturing forest avalanche interaction in PRA models using satellite

151 remote sensing methods that are cost-effective and efficient for processing large scale avalanche terrain models.

3 Methods

Applying the potential avalanche release area (PRA) model to the study area required two main analysis steps. First, developing a pipeline for producing high-resolution DEM and forest classification data from satellite imagery. Second, adapting the existing PRA model to better capture forested terrain and optimizing the input parameters using validation data collected from local avalanche experts. This section describes the open source data processing pipeline for developing high-resolution input data sets, the methods for incorporating a forest land cover classification into the PRA model, and the development of a quantitative accuracy assessment utilizing local validation data to optimize the PRA model for our study area.

3.1 Study area

The study area for this research is the tenure area of CMH Galena, a mechanized skiing operation that operates in the Selkirk Mountains of British Columbia, Canada, approximately 100 km southeast of Revelstoke (Figure 1). The tenure covers 1162 km^2, ranges from 450–3,050 m in elevation and is composed of roughly 60% forested terrain. The Selkirk Mountains have a transitional snow climate with a maritime influence where persistent avalanche problem types are common. The most common persistent weak layers associated with these avalanche problems are surface hoar and faceted crystals associated with a crust (Hägeli and McClung, 2003; Haegeli and McClung, 2007; Shandro and Haegeli, 2018).
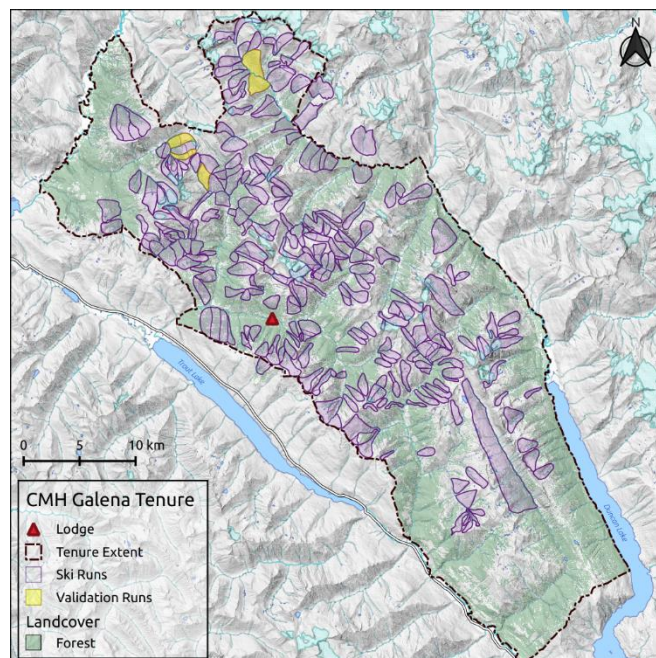
Figure 1. Study area map showing the extent of the CMH Galena tenure, lodge location, operational ski runs, and the subset of runs used to validate the PRA model. Forest data created using Planet Labs RapidEye imagery (Planet Team, 2017).

170

Data preparation

The Bühler et al. (2018) PRA model requires a high-resolution DEM (5 m) and forested land cover classification (5 m). The best existing DEM and land cover datasets for the study area are the Canadian Digital Elevation Model (CDEM) and the 2015 National Land Cover Dataset (NLCD). The resolution of both these datasets is too coarse for high-resolution PRA modelling, with the CDEM at 18 m and the NLCD at 30 m.

Since high-resolution DEMs and forested classification data are still rare in mountainous terrain in Canada, and worldwide, we developed a processing pipeline to create high-resolution versions of these datasets using satellite imagery. The following sections will describe our processing workflow. For a more detailed description of the methods see the supplementary material and to view our processing scripts visit our Open Science Framework (OSF) directory (Sykes et al., 2021).

3.2.1 DEM generation

Based on our desire to develop a cost-effective and reproducible approach for applying PRA models across large areas, we chose to purchase raw satellite imagery and use open source photogrammetry software to produce our own DEM. One downside of this approach is that the vegetation cover inhibits the ability to create a bare ground DEM (known as a digital terrain model; DTM) and we end up with a digital surface model (DSM) that represents the reflective surface at the top of the vegetation. While a DSM is not the ideal representation of terrain in forested areas (Brožová et al., 2020), the high cost of LiDAR, the only remote sensing method that can produce a DTM in vegetation covered terrain, currently prevents its widespread use.

Producing a 5 m DEM requires satellite imagery with a spatial resolution of at least 1.5m. After comparing the products from various providers (Pleiades 1, Worldview 1–4, GeoEye 1, SPOT 6/7, and KOMPSAT 2–3) we purchased SPOT 6/7 imagery based on our requirements of DEM resolution, study area size, and cost. The SPOT 6 tri-stereo satellite images were captured on August 19th, 2019 with 1.5% cloud cover and no visible atmospheric distortions (wildfire smoke, haze) in the images. Tri-stereo imagery captures forward, nadir, and backward looking images in a single pass and provides three stereo image perspectives which increases DEM accuracy in steep terrain and minimizes sensor shading.

To improve and assess the accuracy of our DEM we collected a set of 66 ground control points (GCP) distributed across our study area using a Trimble Geo7x handheld differential global navigation satellite system (DGNSS) unit connected to an H–star base station network, from August 24–27th 2019. We collected GCP in locations with high contrast such as edges of snowfields, water body inlets, bridges, and land cover transitions (e.g., boundary of talus slope and vegetation) to make the locations accurately identifiable in the satellite imagery. The timing of our image collection (August 19th, 2019) and GCP data collection (August 24–27th, 2019) meant that there were minimal changes in the natural features we used as reference points (i.e., snowfields, water bodies).

201 To process the imagery, we used a combination of open source software tools from Geospatial Data Abstraction Software
202 Library (GDAL), QGIS, and the Ames Stereo Pipeline (ASP) version 2.6.2 (Beyer et al., 2018; GDAL, 2021; QGIS, 2021).
203 Several steps of preprocessing were necessary to optimize our images prior to stereophotogrammetry, including bundle
204 adjustment and orthorectification (Shean et al., 2016). The ASP stereo tool was developed for imagery containing bare rock
205 and glacial landscapes. Differences in image texture in forested terrain are challenging for the default settings of ASP to
206 produce accurate pixel matches. To address this issue, we extensively tested different stereo correlation algorithms and stereo
207 processing settings to optimize performance for forested mountainous terrain. Our best results were achieved using the smooth
208 semi–global matching (MGM) stereo correlation algorithm (Facciolo et al., 2015). Optimizing the settings of the ASP stereo
209 tool produced accurate pixel matches in forested terrain and was only limited by artifacts in the original imagery (cloud, cloud
210 shadow, poor lighting conditions).

211 Our stereo processing workflow generated 6 separate DSMs from the SPOT 6 tri–stereo imagery by taking all possible
212 combinations of left and right stereo images. The goal of this method was to reduce DSM holes in steep or poorly lit terrain
213 by taking advantage of the multiple view angles provided by the tri–stereo imagery. Before combining the individual DSMs
214 to produce the final DSM mosaic, we removed pixels with a triangulation error greater than the resolution of the input images
215 (1.5 m) to ensure robust elevation estimates (Figure 2a). Overall, we see low normalized median absolute deviation (NMAD)
216 values across the DSM mosaic (Figure 2b), with a median NMAD of 0.32 m.

217

218
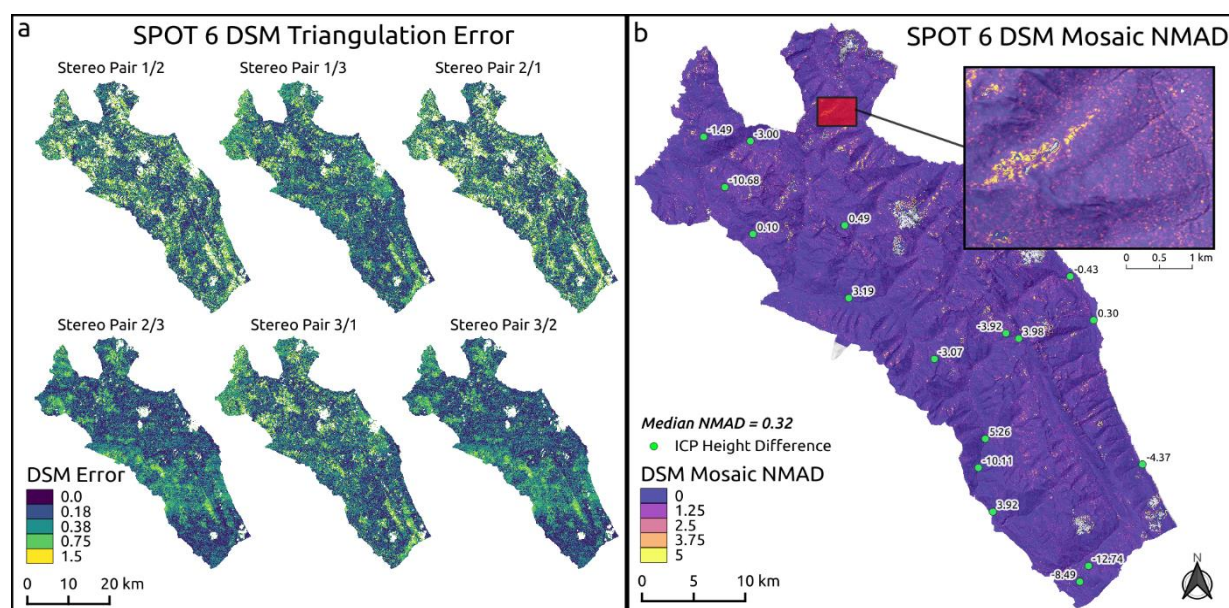
219 **Figure 2. SPOT 6 DSM error estimates. Triangulation error for each set of stereo pairs (a) with pixels where error is greater than**
220 **image resolution (1.5 m) removed from DSM. Normalized median absolute deviation (NMAD) for mosaic of 6 stereo pairs (b) with**
221 **inset map showing slope scale detail. Internal checkpoints (green points) with height difference between DSM surface and DGNSS**
222 **measurement.**

223

224 To improve the alignment of the final DSM mosaic to our GCP, we used the ASP point cloud alignment tool to co–register

225 the output DSM to the GCP (Shean et al., 2016). To evaluate the accuracy of our DSM we used 15 internal checkpoints which

226 were not used as part of our GCP dataset (Höhle and Höhle, 2009).

227 Localized cloud cover and poor lighting on steep north facing terrain caused several holes in our SPOT6 DSM mosaic. We

228 filled these holes by down sampling the existing CDEM to 5m, aligning the CDEM to our SPOT6 DSM mosaic using the point

229 cloud alignment tool in ASP, and then blending the two DEM datasets together. To avoid smoothing the entire SPOT6 DSM

230 we progressively blended the datasets across a 60 m buffer from holes in the SPOT 6 DSM.

231 The methods described here were only tested on a single set of SPOT 6 tri–stereo images, but the performance in forested

232 terrain was vastly improved compared to the default ASP settings. For more detailed information on the ASP workflow or the

233 computer resources used to calculate the DSM please see the supplementary material or contact the authors.

3.2.2 Forest classification

235 The existing PRA model of Bühler et al. (2018) uses a binary forest mask based on photogrammetric vegetation height model

236 classification to mask release areas in forested terrain. We tested several approaches to generate a binary forest mask for our

237 study area. Since our SPOT 6 imagery was limited by poor lighting conditions on steep north facing terrain due to early

238 morning sun angle, we substituted Planet Labs' RapidEye imagery, collected on July 14th, 2018 (Planet Team, 2017). An

239 advantage of the RapidEye imagery is that it includes a red edge band which provides additional spectral resolution to

240 differentiate between forests and other types of vegetation (Dash et al., 2016).

241 To perform the classification, we used the python libraries Numpy, GDAL, Rasterio, and SciKit Learn (GDAL, 2021; Gillies

242 et al., 2013; Harris et al., 2020; Pedregosa et al., 2011). We used a random forest algorithm on the blue, green, red, red edge,

243 and near infrared image bands. In addition, we included the normalized difference red edge index (NDRI), normalized

244 difference vegetation index (NDVI), and normalized difference water index (NDWI). We created training data by manually

245 drawing polygons around individual land cover types (forest, water, bare ground, snow and ice, shrub, moss and lichen) based

246 on RapidEye, SPOT6, and Google Earth imagery from our study area. Our training dataset is composed of 253 individual

247 polygons (12.0 km^2), with 73 polygons of forested terrain (3.6 km^2). For the analysis, we converted the polygons to a binary

248 raster dataset with 144,903 forested pixels and 334,441 non–forested pixels, and randomly split the training data set into equal

249 parts for training and testing of the random forest classifier. To determine the optimal hyperparameters for the random forest

250 model we used a randomized search cross validation (Kuhn and Johnson, 2013). We used a fivefold cross validation with ten

251 iterations and scored based on the accuracy of the classification to select the optimal parameters. Our python script to produce

252 the forest land cover classification is available in the OSF directory (Sykes et al., 2021).

253 **Integration of forest information into PRA model**

254 Our development of additional PRA model functions to improve performance in forested terrain was guided by two principles;

255 1. Minimize additional complexity when running the PRA model compared to the original version. 2. Utilize remote sensing

256 datasets that are available in data sparse locations and do not require extensive field validation.

257 To integrate forest information into the PRA model, we created two additional input parameters: an ordinal *forest density*

258 (Open – 0, Sparse – 1, Moderate – 2, Dense – 3, Very Dense – 4) and a numeric *forest slope scalar* (0.0–2.0). The *forest density*

259 parameter controls what classes of forest are included in the PRA model, while the *forest slope scalar* adjusts the *slope angle*

260 *minimum* threshold based on the *forest density* class for each pixel. If the *forest density* parameter is set to 0, then the *forest*

261 *slope scalar* parameter is not applied. Otherwise, the value of the *forest slope scalar* is determined by the *slope angle minimum*

262 input parameter and *forest density* value. Including these parameters takes advantage of the existing forest mask functions of

263 the PRA model and only adds two input parameters to the model input.

264 **3.3.1 Forest density**

265 To estimate forest density, we used a focal function to calculate the total number of forested pixels within a five–cell

266 neighborhood (625 m^2). We included this step to capture the fuzzy transition between forested and non–forested snowpack

267 characteristics. In areas adjacent to forested terrain the snowpack can be altered by forest cover (i.e., wind dynamics, radiation

268 balance, canopy snowfall interception) despite not being directly covered by the forest canopy (Bebi et al., 2009). This method

269 also helps to identify glades or meadows within the forest canopy by creating a fuzzy buffer around small non–forested islands

270 within densely forested terrain. The size of the neighborhood function (625 m^2) is representative of small human triggered

271 avalanches that have the potential to bury or injure a person, especially if they are carried into a forested area (Schweizer and

272 Lütschg, 2001). This step resulted in a forest sum raster with values ranging from 0 to 25, with 0 meaning no forested cells

273 and 25 meaning all cells within the five–cell neighborhood are forested (Figure 3).

274
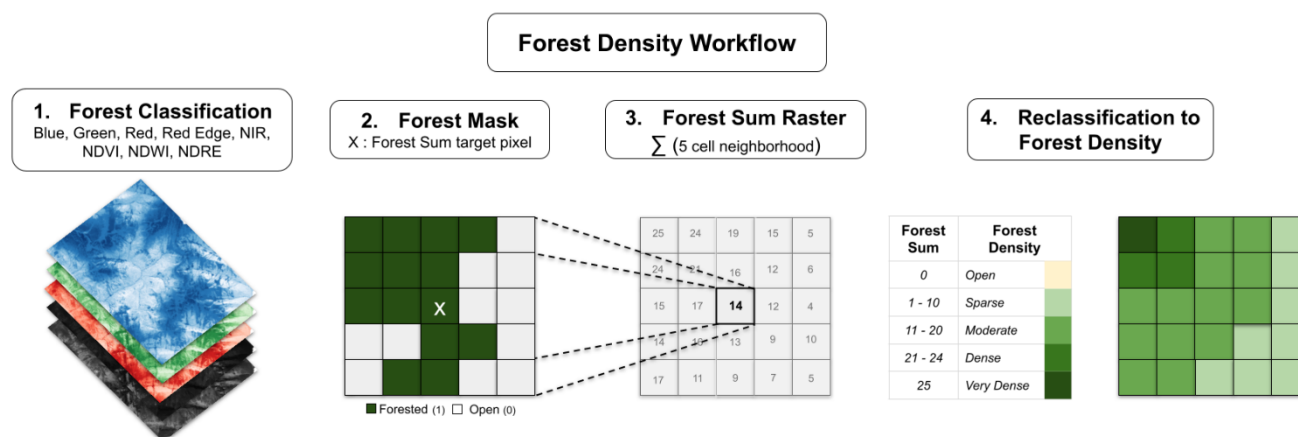
Figure 3. Forest density layer processing workflow.

We then reclassified each forest sum cell into an ordinal variable with the *forest density* categories open (0 cells), sparse (1–10 cells), moderate (11–20 cells), dense (21–24 cells), and very dense (25 cells) (Figure 3). We chose this uneven classification scheme to bias the application of the *forest slope scalar* parameter towards increasing the *slope angle minimum* more strongly in densely or very densely forested areas (i.e., cells with 21 to 25 neighboring forested cells). Since areas with more surrounding forested pixels likely represent more mature forests, this approach captures the fact that more mature forests have a greater potential impact on avalanche release. The resulting *forest density* layer provides a foundation to control how forested cells are included in the PRA model.

2.3.2 *Forest slope scalar*

As an additional control on how the PRA model is applied in forested terrain, we introduced a *forest slope scalar* parameter to increase the *slope angle minimum* based on the *forest density* value. Applying this parameter assumes that steeper slopes are necessary to release avalanches in forested terrain, which is supported by prior research (Campbell and Gould, 2013; Schneebeli and Bebi, 2004). The rate of slope angle increase is controlled by the *forest slope scalar* parameter (0.0–2.0), which is applied as an exponent to the *forest density* value (0–4) and added to the *slope angle minimum* value (e.g., 30°). For example, a *slope angle minimum* of 30° and a *forest slope scalar* value of 1 would result in the following *slope angle minimums* for forested terrain: open (0) 30°, sparse (1) 31°, moderate (2) 32°, dense (3) 33°, very dense (4) 34°. Whereas, a *slope angle minimum* of 28° and a *forest slope scalar* value of 2 would result in the following *slope angle minimums*: open (0) 28°, sparse (1) 29°, moderate (2) 32°, dense (3) 37°, very dense (4) 44° (Figure 4).
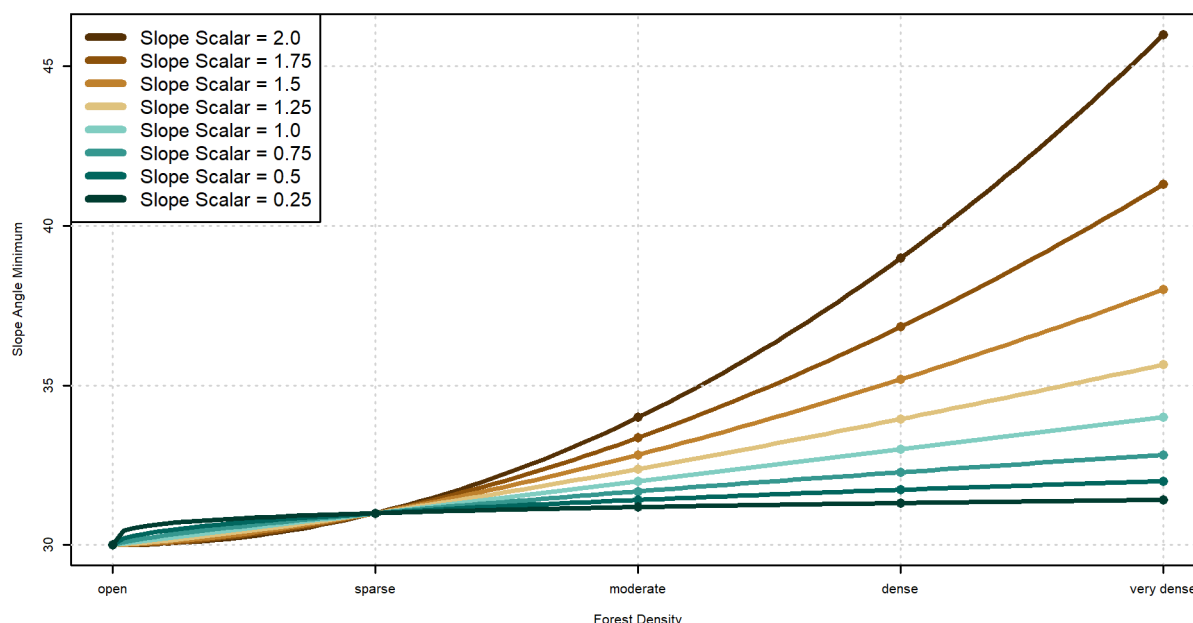
Figure 4. *Forest slope scalar* functions applied to a 30° minimum slope angle threshold.

Parameter tuning and validation

When developing a new version of a PRA model or applying it to a new area, long-term records of spatially accurate avalanche observations that support a standard validation approach as described in Bühler et al. (2018) might not always be available. However, local avalanche safety experts such as mountain guides can have extensive knowledge about local avalanche activity patterns. To determine the optimal parameter settings and assess the performance of our PRA extension into forested terrain, we developed a novel method that takes advantage of this type of expertise and collaborated with two CMH Galena guides who each have decades of experience in our study area.

3.4.1 Validation data collection

CMH Galena primarily operates on approximately 300 defined ski runs within their tenure. The runs range in size from 0.2–19.0 km² and their locations have been mapped with polygons that outline the typical skiing terrain (Figure 1). The frequency of how often these runs are used varies significantly depending on terrain characteristics, weather conditions for flying, and snowpack conditions. To validate the PRA model, the two collaborating guides selected five runs based on their familiarity

310   with the terrain and the balance of forested and alpine avalanche terrain contained in the runs (highlighted validation runs in

311   Figure 1).

312   Since mapping the precise location of start zones based on personal recollection without being in the terrain at the time is

313   extremely difficult, we developed a workflow that would explicitly accommodate this uncertainty. Instead of forcing the

314   participating guides to explicitly outline all avalanche release areas, our data collection workflow asked them to draw validation

315   polygons in a map interface that contain terrain of consistent character and specify for each polygon what proportion represent

316   potential release areas (0%, 25%, 50%, 75%, 100%) (Figure 5). Polygons of obvious probable release areas or non–release

317   areas where guides had high confidence about their spatial extent were labeled with 100% and 0% respectively. Areas with

318   scattered probable release areas, such as open forests with glades, where the identification of each probable release area would

319   be cumbersome and unreliable, were marked as larger polygons and labelled with the estimated spatial proportion of the

320   probable release areas (25%, 50% or 75%). Release areas that require specific snowpack structures and weak layer types (e.g.,

321   surface hoar) were minimized in the validation dataset in order to focus avalanche release types that occur more frequently.

322   The process of collecting validation polygons from the CMH guides was carried out on a custom designed website. The website

323   platform enabled us to develop and present meaningful reference layers (e.g., satellite imagery, topo maps, terrain data, GPS

324   tracks, heat maps) and provide the guides with multiple perspectives of the study area to assist with drawing the validation

325   polygons. Both guides drew release area polygons for the five validation runs individually before creating a final consensus

326   set of polygons in collaboration.

327   Our fuzzy approach to mapping probable release areas has several advantages. Foremost, accommodating uncertainty in the

328   spatial extent of release areas is a requirement when relying on human memory to generate the validation data as specifying

329   probable release areas with higher precision from memory is simply unrealistic. This method also accounts for the variability

330   in release area extent that results from the dynamic nature of snowpack and weather conditions. The workflow also minimizes

331   the effects of local errors in the reference layers that we provided the guides with to record their validation polygons. Specific

332   examples of uncertainty caused by reference layers are variations in satellite imagery lighting due to sun angle and artifacts of

333   the DSM generation process, such as over steepened slope angle values caused by transitions from forested to non–forested

334   terrain.

335
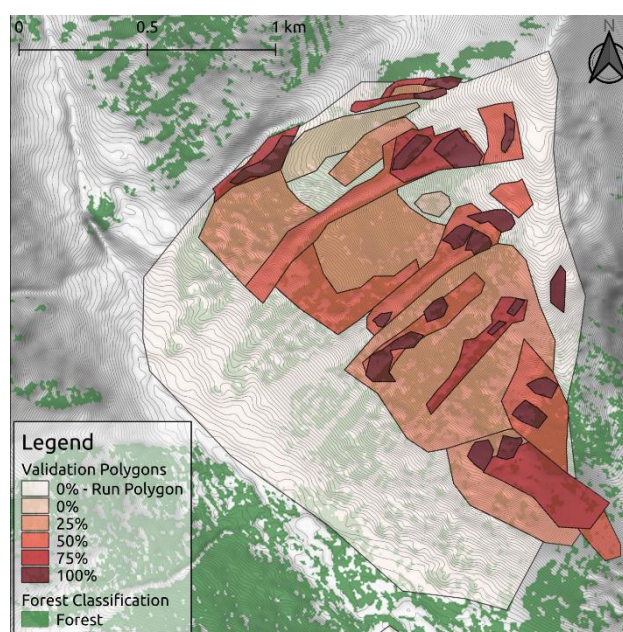
Figure 5. Validation polygons from one run at CMH Galena. Polygons are color coded based on the release area proportion of each polygon. Forest data created using Planet Labs RapidEye imagery (Planet Team, 2017).

Our final validation dataset consists of 167 polygons across five runs with a total area of 8.42 km^2. In locations where the polygons overlapped, we retained the highest proportion value of the overlapping polygons. The overlapping region was also clipped from the total area of the lower probability polygon. Locations within the run polygons that were not explicitly mapped by the guides were assumed not to be release areas. However, our validation approach differentiates between these implied and the explicit 0% validation polygons because we have more confidence in the latter.

3.4.2 PRA model grid search

In contrast to the raster based validation approach of Bühler et al. (2018), our validation dataset requires analysis on the scale of individual polygons. Since we do not know the explicit locations of the release areas in polygons with release area proportions of 25%, 50%, or 75%, we cannot directly compare the PRA model output to the validation polygons on a pixel-by-pixel basis. Instead, we have to compare the total area within each polygon that is considered a PRA by the model to the proportion provided by the local guides. To calculate the error between the model and the guides' assessment for each polygon, we subtracted the proportion of the area of each polygon that the PRA model determines as a release area from the release area proportion determined by the guides. This *PRA error* value is the basis of our grid search process.

To properly reflect the validation data collection process in our analysis we also need to consider the hierarchical structure of assessment polygons collected from the local guides. The highest value validation data are the 100% and 0% polygons because

355 they provide explicit spatial extents for PRA locations. These polygons are from locations the participating guides are most

356 familiar with and have the highest level of confidence in. We therefore placed more emphasis on PRA model performance in

357 these areas when selecting the optimal inputs. The validation polygons with the greatest uncertainty are the run polygons. They

358 were not explicitly drawn by the guides and the absence of PRA within these polygons was implicit and not explicitly specified.

359 Hence, the accuracy of these polygons was weighted least in selecting the optimal PRA input parameters.

360 To select optimal input parameters for the PRA model we performed a grid search as described by Bühler et al. (2018) using

361 the following values: *slope angle minimum* (default 30°, range 20°–40°), *slope angle maximum* (default 60°, range 45°–65°),

362 *ruggedness window* (default 9, range 3–15), *ruggedness maximum* (default 6.0, range 0.5–10.0), *curvature maximum* (default

363 6.0, range 0.5–10.0), *forest density* (default NA, range 0–4), *forest slope scalar* (default NA, range 0.0–2.0) (Table 1). We

364 used a set of default parameters from Bühler et al. (2018) as a baseline and iterated over each parameter to analyze the impact

365 on the accuracy of the model. The input parameters *slope angle minimum, slope angle maximum, ruggedness window,*

366 *ruggedness maximum,* and *curvature maximum* are derived from the DEM (Figure 6 a–c). The *forest density* input parameter

367 is derived from the forest mask (Figure 6d).

368 **Table 1. Grid search input parameter values**

Input Parameter	Range	Interval	Default	Optimized
Slope Angle Minimum	20°–40°	1°	30°	*Yes*
Slope Angle Maximum	45°–65°	1°	60°	*No*
Ruggedness Window	3–15	2	9	*No*
Ruggedness Maximum	0.5–10.0	0.5	6.0	*No*
Curvature Maximum	0.5–10.0	0.5	6.0	*No*
Forest Density	0–4	1	NA	*Yes*
Forest slope scalar	0.0–2.0	0.25	NA	*Yes*

369

370 Selecting the optimal set of input parameters did not rely on any single statistic. Each PRA model iteration was compared

371 using the mean absolute error (MAE), mean bias error (MBE), proportion of accurate polygons, and proportion of

372 underestimated and overestimated errors. MAE values can range from 0 to 100, with lower values indicating a more accurate

373 model. MBE values can range from -100 to 100, with 0 indicating a balance between positive and negative errors.

374 Underestimated and overestimated polygons are defined as having a PRA error greater than ± 12.5%, because the validation

375 polygon release area proportion bins have a range of 25%. Polygons with a PRA error greater than ± 25% were considered

376 severely overestimated or underestimated.

377 The accuracy statistics for each grid search iteration were calculated on the basis of the total number of polygons (n = 167).

378 We elected not to weight the statistics based on polygon size because the highest value validation polygons (0% and 100%)

379 are generally the smallest. Selecting the optimal input parameters for our PRA model required evaluating performance across

380 all these statistics and taking the structure of our validation dataset into account.

381 When selecting the optimal set of input parameters we erred on the side of a model that overestimates the extent of potential

382 avalanche release areas, which is indicated by a negative MBE. We consider this an appropriate approach because the guides'

383 polygons reflect only the avalanche conditions that they have experienced and recall. Despite their multiple decades of

384 experience, the guides have not witnessed all potential combinations of snowpack conditions, which could cause avalanche

385 release in uncommon areas. In contrast, the PRA model is a terrain based tool which aims to identify locations in the study

386 area which have the potential for avalanche release independent of snowpack conditions.

387

388
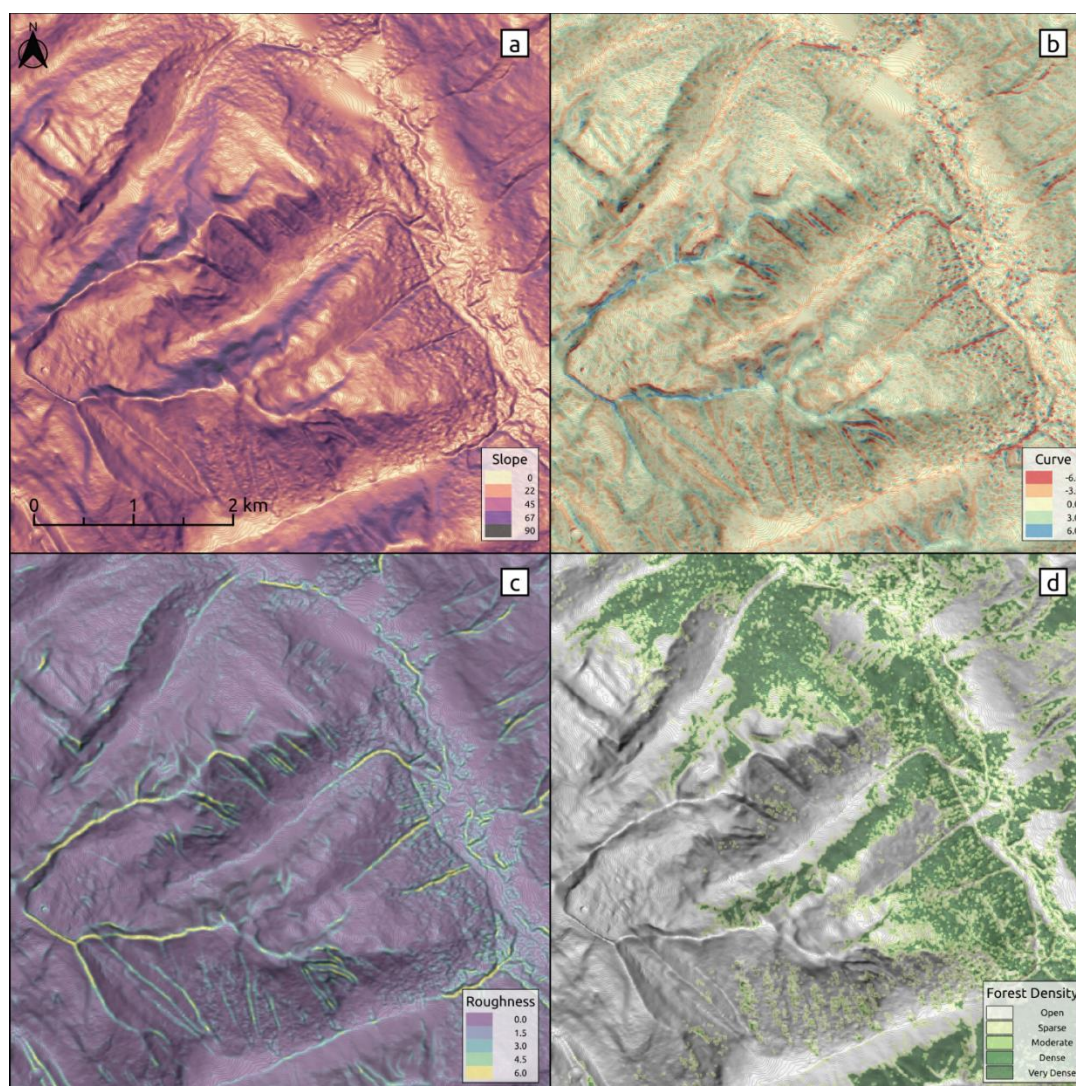
Figure 6. PRA model input parameters. *Slope angle, curvature*, and *ruggedness* derived from the DEM (a–c) and *forest density* derived from the forest mask (d). Forest data created using Planet Labs RapidEye imagery (Planet Team, 2017).

391

4 Results and discussion

Since the context of the input data, parameter settings, and output from the original model are vital for evaluating the performance of our updated version of the PRA model, we combine the results and discussion into a single section. After presenting and commenting on the results, we conclude this section with an evaluation of some likely sources of error for our updated PRA model and share our thoughts on the limitations of a purely satellite remote sensing based method for capturing forest character in the PRA model.

4.1 Data preparation pipeline

The data preparation pipeline produced a 5m resolution satellite DSM and forested land cover data set as input for the PRA model. Using 15 internal check points (ICP), the DSM accuracy can be described with a median vertical error of -0.43 m and normalized median absolute deviation (NMAD) of 4.72 m (Table 2). These accuracy metrics indicate good performance of the stereo DSM method, especially considering the rugged mountainous terrain across our study area and close proximity of steep slopes to some of the ICP. Compared to the best available existing DEM for our study area (18 m resolution CDEM), the SPOT 6 DSM provides vastly improved small scale terrain feature identification (Figure 7).
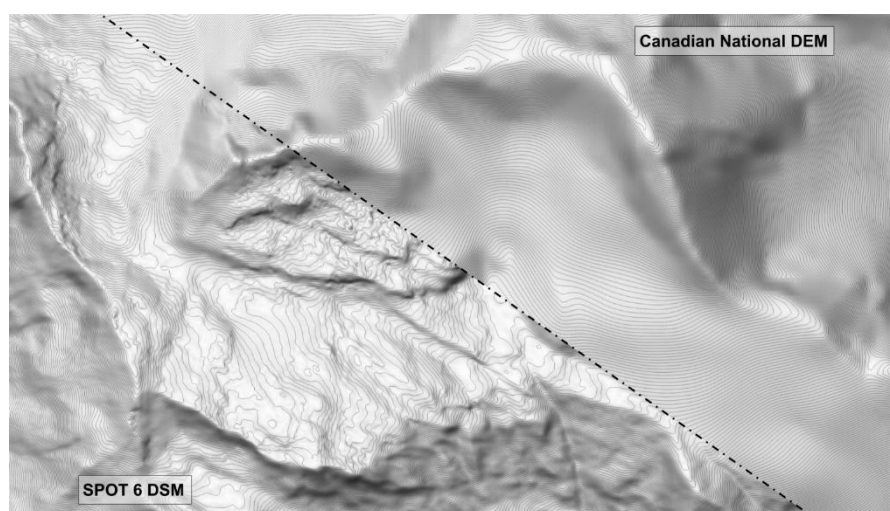
Figure 7. Comparison of existing 18 m resolution CDEM to 5 m resolution SPOT6 satellite stereo DSM, derived from our data preparation pipeline.

Table 2. Accuracy statistics for SPOT6 satellite stereo DSM based on 15 ICP.

Metric	Error Type	Value (m)
Median	Δ h	-0.43
NMAD	Δ h	4.72
68.3% quantile	|Δ h|	3.96
95% quantile	|Δ h|	9.25

The forested land cover classification that emerged from our random forest analysis yielded an overall accuracy of 98.88% based on 253 training polygons (12.0 km^2). The training polygons were rasterized and split randomly into training and testing data sets composed of 239,672 pixels each. We also calculated the area under the receiver operating characteristic curve (AUC) to compare true positive rate and false positive rate of the classification and found an area of 99.89%. The classification feature importance showed heavy reliance on the red edge (59.8%), NDWI (15.2%), and green (14.9%) bands.

The overall accuracy of the classifier is critical for providing a distinction between forested land cover and other types of vegetation, such as shrubs and herbaceous plants. For avalanche release area modelling this distinction is important because shrubs and herbaceous plants are buried or pressed down beneath the winter snowpack and therefore have minimal effect on the potential for avalanche release. Trees with rigid trunks that resist being laid over by the winter snowpack and canopy heights greater than the snowpack depth (approximately 2–3 m) have an anchoring effect on the snowpack which is essential to capture accurately in order to account for their effect on avalanche release.

Creating the forested land cover classification using the same satellite imagery as the stereo DSM processing would be the most efficient workflow for producing the necessary input data sets for PRA modelling, because it uses the least possible input data and thereby minimizes data acquisitions costs and effort. However, in our study, we elected to utilize Rapid Eye imagery as an alternative due to better overall lighting conditions and improvements in accuracy, primarily due to the red–edge spectral band. The overall accuracy of our classifier and the feature importance of the red edge band highlight the strength of RapidEye imagery for forest classification modelling.

Our processing pipeline provides a cost-effective approach for creating high-resolution DEM and forested land cover classification data in remote and data sparse regions. Compared to alternative methods, such as LiDAR and commercial satellite stereo DEM products, purchasing raw satellite stereo imagery to produce a high-resolution DEM provides significant cost savings, control over the DEM generation settings, and produces a DEM product with sufficient accuracy (Kramm and Hoffmeister, 2019; Shean et al., 2016). The primary limitations are the inability to resolve bare ground terrain features, susceptibility to DEM holes due to cloud cover and lighting conditions, and degree of technical knowhow and computer

435 processing resources required to convert the raw imagery to a DEM product. Despite these limitations, the processing pipeline

436 enhances accessibility for high-resolution PRA modelling in remote regions.

4.2 Model parameter selection based on grid search

438 Based on the grid search we determined the optimal model input values for our study area are: *slope angle minimum* 27°, *slope*

439 *angle maximum* 60°, *curvature maximum* 6.0, *ruggedness window* 9, *ruggedness maximum* 6.0, forest density 4, and *forest*

440 *slope scalar* 1.25. The grid search method that we implemented is based on a set of default input parameters and does not

441 calculate all possible combinations of input parameters in order to reduce the amount of computer resources necessary.

442 Therefore, the results of the grid search are dependent on the selected default parameters. We tested a wide range of potential

443 default parameters for our grid search and used the values from Bühler et al. 2018 as a starting point. We selected the optimal

444 values by visualizing the distribution of the *PRA error* and plotting the MAE and MBE values for each grid search iteration

445 (Figure 8).

446 Due to the high quality and long-term avalanche observation records used for validation in Bühler et al. 2018, we retained their

447 default parameter values if the grid search did not demonstrate notable improvement in overall accuracy based on the local

448 validation dataset. This was the case for *slope angle maximum, ruggedness window*, *ruggedness maximum,* and *curvature*

449 *maximum*. The results of our grid search for these parameters are similar to those shown in Figure 3 of Bühler et al 2018, with

450 relatively low variation in accuracy across the range of grid search values (Figure 8, panels b to e). The consistency of these

451 input parameters for both Davos and Galena are likely due to using the same DEM resolution of 5m and points to the

452 universality of the physical characteristics necessary for avalanche release. In addition, this consistency is a testament to the

453 accuracy of our satellite DSM in comparison to the high-resolution DEM data used in the Davos research.
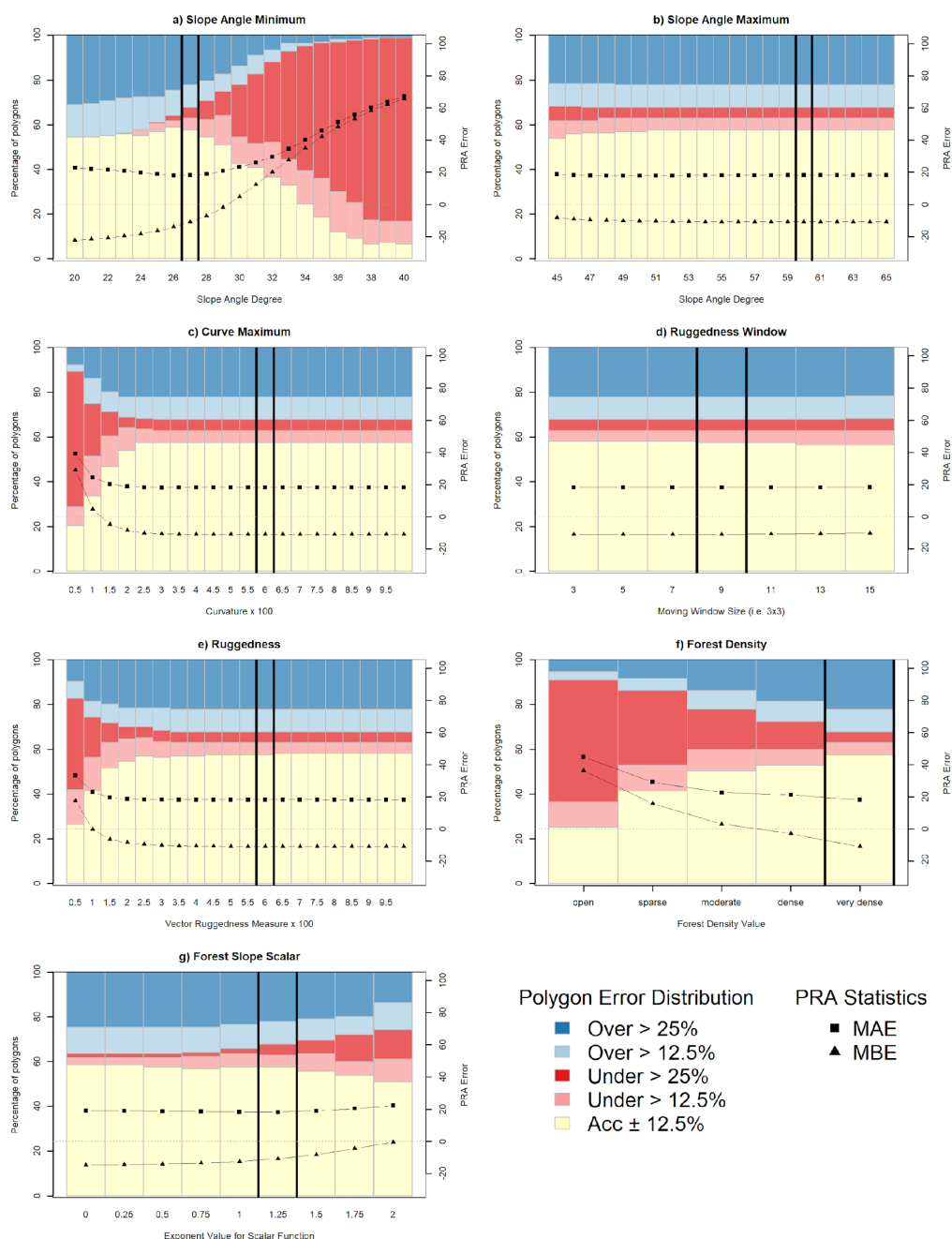
Figure 8. Results of PRA model grid search. In each of the panels, the left Y–axis shows the percentage of polygons in different PRA error classes with colored bars (accurate – yellow, underestimated – red, overestimated – blue). Black squares and triangles show the values of MAE and MBE for each grid search iteration with a grey dashed horizontal line to show the 0 threshold which correspond to the right Y–axis. The vertical back lines indicate the optimized parameter settings.

4.2.1 Slope angle minimum

Slope angle minimum has the largest impact on the performance of the PRA model. Selecting the optimal input parameter required balancing the performance of the PRA model against the different types of validation polygons and considering our target of a frequent avalanche scenario. When considering the entire validation polygon data set, there is a sharp increase in the percentage of underestimated validation polygons as the *slope angle minimum* threshold increases from 25°, which indicates that the PRA model progressively excludes observed release areas (Figure 8, panel a). The MAE minimum of approximately 18 occurs between 26° and 28°, indicating that these values produce the most accurate versions of the PRA model. The MBE is negative for *slope angle minimum* values below 30° with a steep decrease between 26° and 30°. This shows that decreasing the *slope angle minimum* below 30° creates PRA models that are progressively more biased towards overestimating release areas.

To further analyze the performance of the PRA model we separated the validation polygons based on the validation polygon type. 0% and 100% polygons have the highest accuracy with values of *slope angle minimum* less than 25° (Figure 9, panel a). This trend strongly contrasts the other polygon types (Figure 9, panels b and c), which have higher percentages of accurate polygons for *slope angle minimum* values > 26°. For 0% and 100% polygons the percentage of accurate polygons declines steeply above 26° accompanied by an increase in severely underestimated polygons. The MAE and MBE statistics follow a similar trend, with relatively uniform values until 27° followed by steeply increasing error rates and positive bias for the remaining grid search inputs.
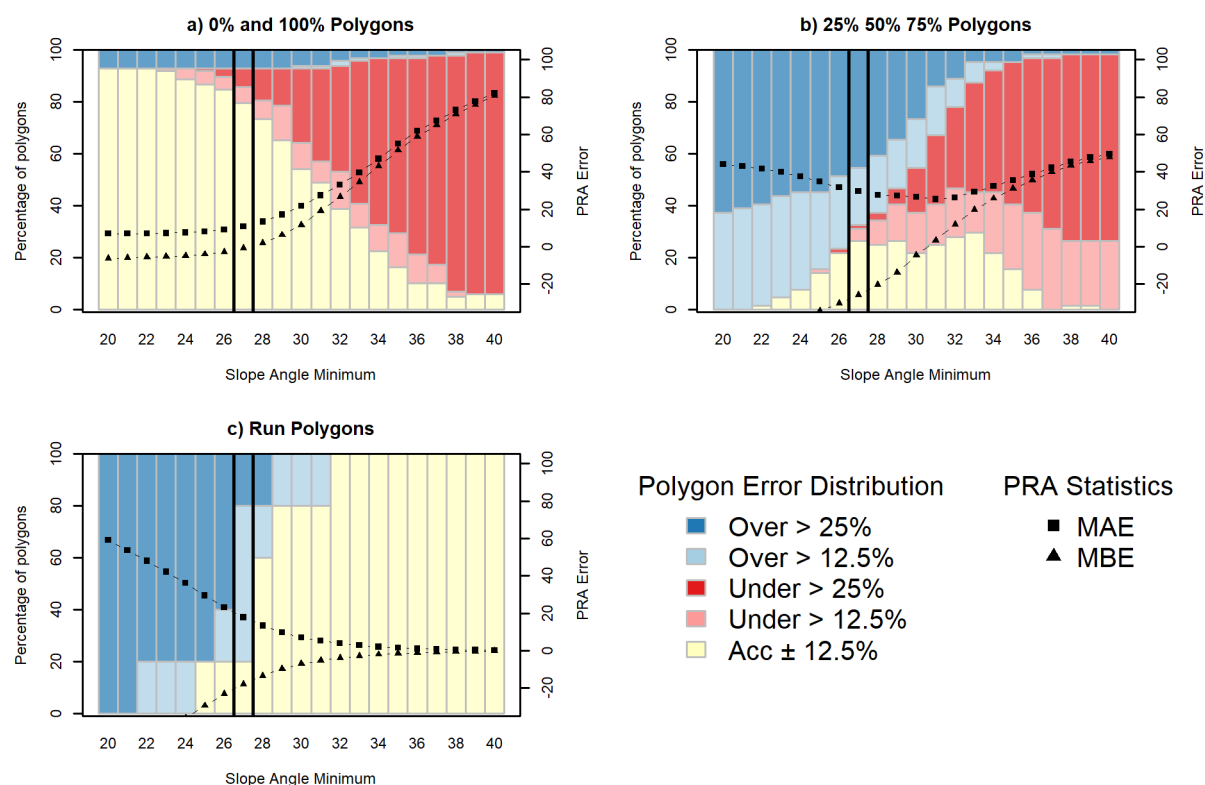
Figure 9. Frequent avalanche scenario PRA model grid search results for *slope angle minimum* with validation polygons split based on the type of polygon.

The 25%, 50%, and 75% polygons (Figure 9, panel b) have a bimodal distribution for percent of accurate polygons, with slight peaks at 27° and 33°, accompanied by a steep increase in underestimated polygons from 27° upward. The MAE values are at their minimum between 27° and 33° with relatively uniform values within that range. Both above and below that range we see increasing MAE values, indicating a less accurate model for this group of polygons. Below 30° the MBE values indicate a negative bias and have a steeply negative trajectory. This shows a strong bias toward overestimating PRA area for 25%, 50%, and 75% polygons at lower values of *slope angle minimum*.

The run polygons (Figure 9, panel c) have the highest accuracy with *slope angle minimum* greater than 31°. However, the percentage of severely overestimated polygons decreases drastically at 27°. Below 28°, the MAE and MBE have steeply increasing error rates and negative biases, respectively. Above 28° the curves flatten out and trend towards 0 for both MAE and MBE.

Our choice of a 27° *slope angle minimum* strikes a balance between PRA model performance for each polygon type with a priority towards optimizing performance on the 0% and 100% polygons, which are the most spatially explicit and have the

493 highest degree of certainty. Setting the *slope angle minimum* lower than 27° would result in too strong of a bias towards

494 minimizing underestimated errors which is not appropriate given our target of a frequent avalanche scenario. This is illustrated

495 by a decrease in overestimated and severely overestimated polygons at a *slope angle minimum* value of 27° for the 25%, 50%,

496 75% polygon dataset as well as the run polygons (Figure 9, panels b and c).

497 **4.2.2 *Forest density* and *forest slope scalar***

498 Determining the optimal value for *forest density* was the most straightforward of the three parameters we optimized because

499 the percentage of accurate polygons, lowest MAE, and lowest proportion of underestimated polygons all occur at *very dense*

500 *(4)* (Figure 8, panel f). Setting *forest density to very dense (4)* means that the PRA model is not restricted by any forest mask

501 and the *forest slope scalar* is applied across the full range of *forest density* values.

502 Out of the three parameters we optimized, *forest slope scalar* has the least variation in percentage of accurate polygons, MAE,

503 and MBE across the range of values tested in the grid search (Figure 8, panel g). This indicates that the PRA model

504 performance is less sensitive to changes in *forest slope scalar* compared to *slope angle minimum* and *forest density*. However,

505 setting this parameter to 1.25 helps to create a more balanced model by decreasing the number of overestimated polygons,

506 which is illustrated in the upward trend of the MBE value.

507 Similar to *slope angle minimum*, we see a decrease in the percentage of severely overestimated polygons for the 25%, 50%,

508 and 75% and run polygon datasets for higher values of *forest slope scalar* (Figure 10, panels b and c). This is a trade off with

509 a slight decrease in the percentage of accurate polygons and increase of percentage of underestimated polygons for the 0% and

510 100% polygons (Figure 10, panel a). This is reflected in the 0% and 100% polygon MBE value of -0.81 at 1.25, which is

511 relatively high compared to the other polygon types. Given our target of a frequent avalanche scenario this trade off is justified

512 to create a balanced PRA model and account for the influence of forested terrain on avalanche release.

513
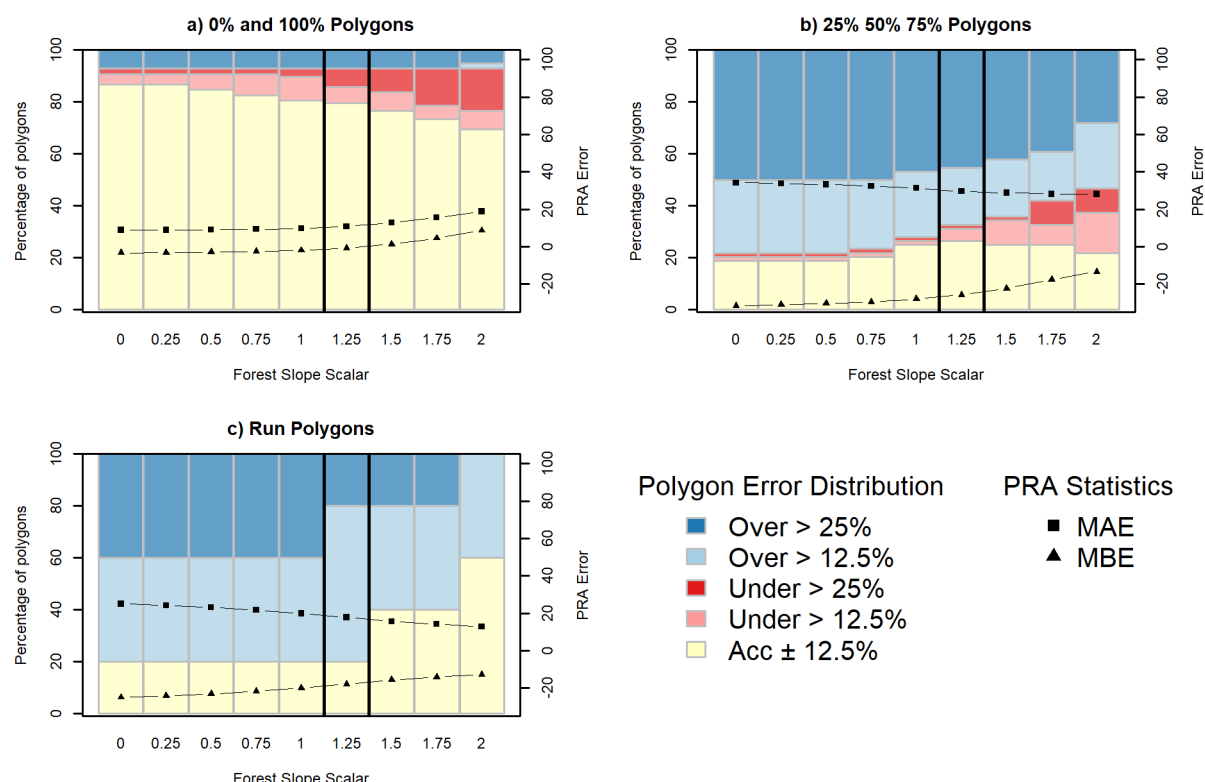
Figure 10. Frequent avalanche scenario PRA model grid search results for *forest slope scalar* with validation polygons split based on the type of polygon.

4.3 PRA model output and comparison

The final PRA model captures 57.5% (96 of 167) of the consensus validation polygon data set accurately, meaning that the PRA model predicted area is within ± 12.5% of the area specified by the guides for each validation polygon (Table 3). The remainder of the validation polygons were either underestimated 10.2% (17 of 167) or overestimated 32.3% (54 of 167), compared to the guides' consensus estimates of release area proportion. The MAE value is 18.2, which is a measure of the average error across all polygons. The MBE value is -10.9, which indicates that the PRA model errors are negatively biased towards overestimating release areas. This interpretation of the MBE value aligns with the skewed distribution of underestimated and overestimated polygons.

Table 3. PRA model comparison

PRA Model	MAE	MBE	Accurate %	Under %	Over %
Present model	18.2	-10.9	57.5	10.2	32.3
Bühler 2018 – Forest Mask	33.1	22.3	31.0	58.3	10.7
Bühler 2018 – No Forest Mask	21.4	-3.7	45.8	25.0	29.1

To evaluate whether our parameter optimization demonstrates meaningful improvement, we compared the accuracy statistics of the model using the optimized parameters (Present model) to the Bühler et al. (2018) defaults both with and without a forest mask (Table 3). The 'Bühler 2018 – forest mask' PRA model does not identify release areas in any terrain identified as forested based on the land cover classification, whereas the 'no forest mask' version allows the PRA model to calculate release areas in all terrain. Since the 'forest mask' version naturally performs substantially worse in most accuracy statistics due to the large proportion of forested terrain in our study area, we will focus the comparison on the 'Bühler 2018 – no forest mask' model version.

Overall, we see improvements in the MAE, percent of accurate polygons, and percent of underestimated polygons using the locally optimized input parameters. The MAE for the present model is 18.2 compared to 21.4 for the 'Bühler 2018 – no forest mask' version, demonstrating a slight improvement in overall model error (Table 3). The present model improves the percent of accurate polygons by 11.7 percentage points over the 'Bühler 2018 – no forest mask' PRA model, which is a substantial improvement. Similarly, the reduction of 14.8 percentage points for underestimated polygons between the present model and the 'Bühler 2018 – no forest mask' demonstrates the improved performance of the grid search optimization. These improvements can be attributed to optimizing the *slope angle minimum* and *forest slope scalar* input parameters using the local validation data

The trade off of the optimized input parameters for the present model is a bias towards overestimation, which is indicated by the MBE of -10.9 compared to -3.7 for the 'Bühler 2018 – no forest mask'. This is also shown by the slight increase of 3.2 percentage points in overestimated polygons from the 'Bühler 2018 – no forest mask' to the present model. Producing a more negatively biased PRA model is in line with our mindset of creating a PRA model that errs on the side of overestimating observed release areas. In our opinion, the benefits of improved percentage of accurate polygons and underestimated polygons outweighs the downside of a slight increase in overestimated polygons.

The present model has a substantially lower *slope angle minimum* of 27° compared to the default value of 30° from Bühler et al. (2018), which results in a notable increase in the overall area of the PRA output due to expansion into lower angle terrain (Figure 11). The fact that the validation data led us to a substantial decrease in *slope angle minimum* is likely due to differences

556 in the terrain and snowpack characteristics in our study area compared to the region of Davos in Switzerland where the model
557 was initially validated. The avalanche character in our study area is prone to persistent avalanche problem types with the most
558 common weak layers being either surface hoar or faceted crystals associated with a crust (Hägeli and McClung, 2003; Haegeli
559 and McClung, 2007; Shandro and Haegeli, 2018). As a weak layer, surface hoar can release at lower slope angles and has
560 increased potential to propagate across terrain features compared to other weak layer types (McClung and Schaerer, 2006).
561 The fact that our validation data set and grid search approach produced a PRA model that also aligns with our theoretical
562 understanding of the snowpack properties in our study area is an encouraging result. However, in terrain within the study area
563 that is not prone to surface hoar development our PRA model is likely to overestimate PRA extent.

564

565
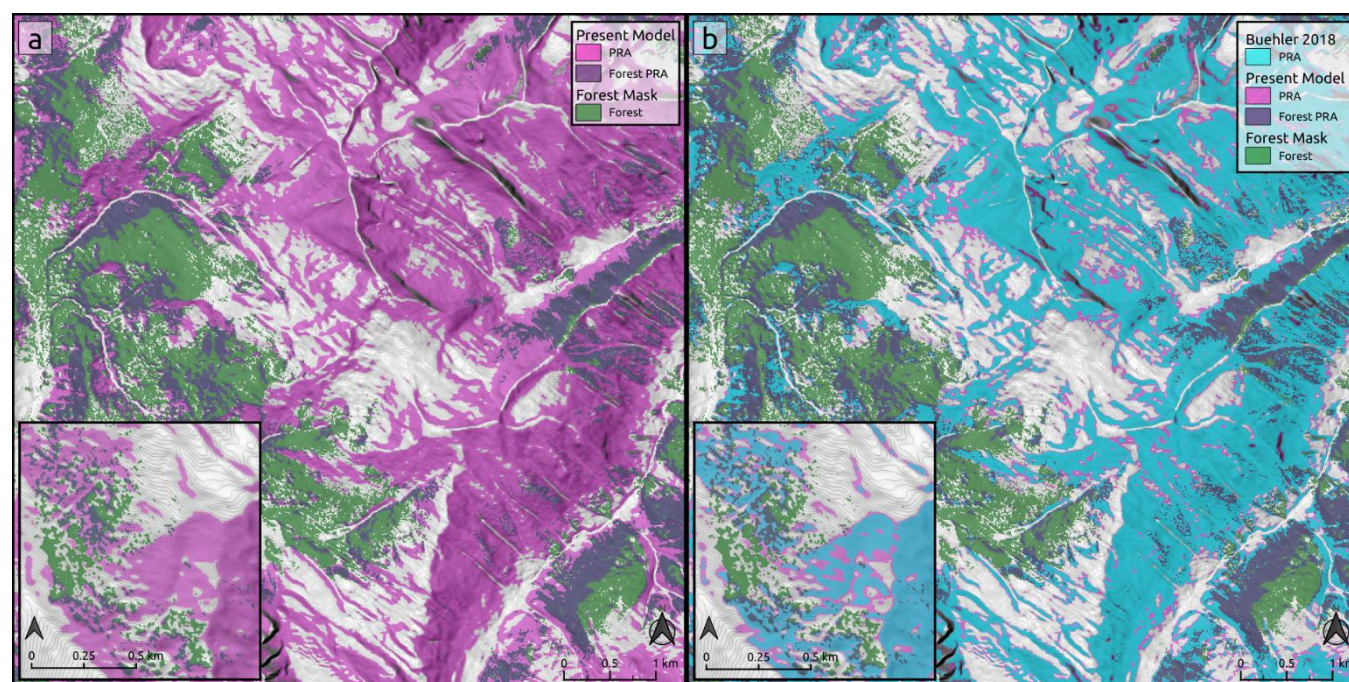
**Figure 11. Comparison of present PRA model (a) to 'Bühler 2018 – forest mask' (b). Present model PRA area is pink with purple
for forested areas. 'Bühler 2018 – forest mask' is shown in blue on panel b for comparison. Inset maps show detailed PRA comparison
on a local scale. Forest data created using Planet Labs RapidEye imagery (Planet Team, 2017).**

569

570 **4.4 Potential sources of PRA model errors**

571 Based on discussions with our collaborating guides and exploring spatial patterns of discrepancies between our validation data
572 set and PRA model output, we have highlighted two likely sources of error in our PRA model. First is the limitation of using
573 a relatively simple remote sensing based approach to account for forested release areas in the PRA model, which does not

explicitly capture forest characteristics that are known to have a strong bearing on the interaction of avalanches and forest, such as crown cover, stem density, and gap size (Bebi et al., 2009; Teich et al., 2012). Second is the inherent uncertainty of relying on human experience to generate validation data, which can be subject to individual biases and faulty recollection. This section provides examples of these sources of error and discusses how we have attempted to minimize their impact on the PRA model accuracy.

4.4.1 Forest characteristics

To shed light on potential sources of PRA model errors we applied two different approaches that consider different spatial scales. First, we visualized the spatial patterns in the PRA errors for each validation run and consulted the local guides to provide their insight. Second, we extracted the terrain characteristics of the entire set of validation polygons and compared the distributions of the terrain characteristics based on the PRA error value. Both approaches yielded similar insight, which highlight the challenge of capturing forested avalanche release areas accurately using an approach based purely on satellite imagery.

Visualizing the patterns of PRA model error by validation run reveals concentrated clusters of higher PRA error on specific runs or subregions within runs (Figure 12). The 'Lunatic Fringe' run has by far the highest proportion of overestimated polygons out of the five validation runs, with 22 out of the 42 validation polygons being overestimated (Figure 12, panel a). Based on information provided by the local guides, this run is characterized by a steep continuous face with several well-defined large avalanche paths dissecting mostly forested terrain. The forest is very dense and impassable for a guided group at the upper elevations of this run. In contrast, the 'Red Baron' run, which is located directly across the valley from 'Lunatic Fringe', contains lower slope angle terrain with a large proportion of mature forest (Figure 12, panel b). The forest has greater canopy height with widely spaced gaps between the individual trees. The forest canopy between each tree extends horizontally enough that the land cover classification is unable to detect many of the gaps on the forest floor. This run contains 7 out of 8 of the severely underestimated validation polygons, with the other polygon located in a forested area with similar characteristics on the 'Bandito' run.
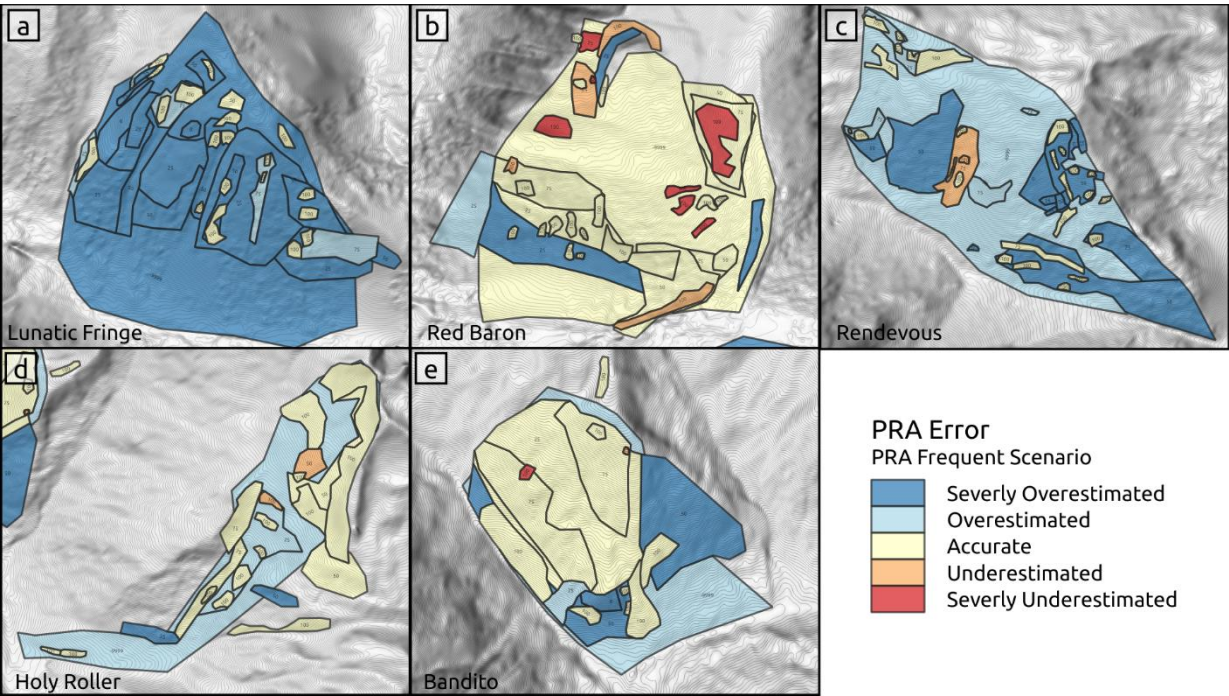
Figure 12. PRA model accuracy for each validation run. The validation polygons are labelled with their release are proportion and color coded based on the *PRA error* for each individual polygon.

While the *forest slope scalar* input parameter is designed to account for the interaction of forest and avalanche release, it is challenging to apply it on these two drastically different types of forested terrain. For 'Lunatic Fringe', increasing the *forest slope scalar* input parameter would improve accuracy by increasing the *slope angle minimum threshold* based on the local *forest density*. However, increasing the *forest slope scalar* would be detrimental for 'Red Baron' because of the potential for avalanche release in forest gaps within densely forested areas. These two contrasting examples of how the PRA model handles avalanche forest interaction highlight the challenge in creating a balanced PRA model which compromises performance in each type of forested terrain.

The guides' descriptions of the local forest character causing PRA errors for 'Lunatic Fringe' and 'Red Baron' are supported by our analysis of terrain characteristics based on the validation polygon dataset. To investigate whether there are common patterns in the terrain characteristics of validation polygons based on their PRA error value we extracted the aspect, curvature, elevation, forest cover, forest density, ruggedness, and slope angle distributions for the validation polygon dataset. While the majority of these terrain characteristics had similar distributions for all classes of PRA error, forest cover percentage and forest density had distinct differences. For 'severely underestimated' polygons the distributions and median values are biased towards higher percentages of forest cover and forest density compared to other PRA error classes (Figure 13).

616

617
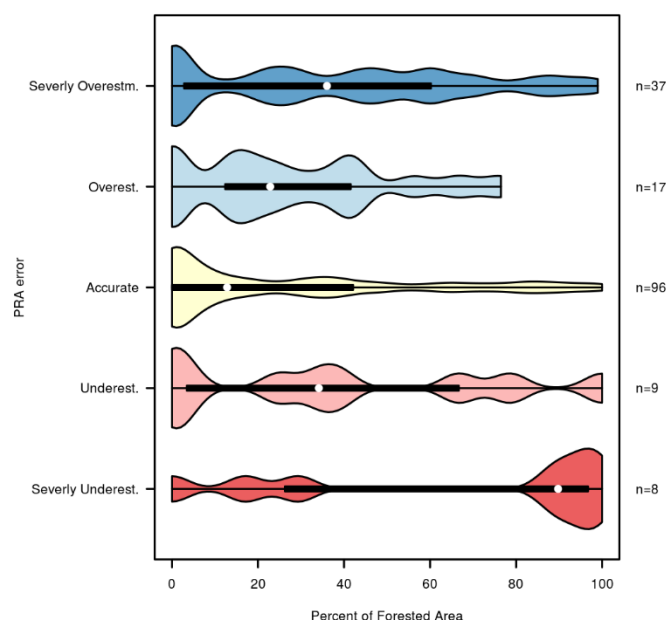
Figure 13. Analysis of PRA error based on percentage of forested area for the validation polygon data set. The plot shows the distribution of forest cover percentage for validation polygons based on their PRA error.

620

This further illustrates the guides' interpretation that the severely underestimated polygons on 'Red Baron' have high forest density and the limitation of our *forest slope scalar* approach for accounting for forested terrain with highly variable characteristics. It is important to note that the sample size of 'severely underestimated' polygons is small with only eight polygons. For context, the distribution 'severely overestimated' (n = 37) polygons also include high percentages of forest cover and forest density, which can be partially attributed to the dense and tightly spaced forested terrain on 'Lunatic Fringe'.

The PRA errors on 'Lunatic Fringe' and 'Red Baron' demonstrate the limitations of our approach in capturing the real world forest characteristics. Improving the performance of the PRA model in forested terrain would require more detailed data sets such as LiDAR or a field based forest inventory which could capture additional forest characteristics such as stem spacing (Ginzler and Hobi, 2015; Waser et al., 2015; Wallner et al., 2015; Rahimizadeh et al., 2020; Hyyppä et al., 2000; Dash et al., 2016), which are beyond the scope of this research. The benefit of our method is to create cost-effective and high-resolution avalanche terrain maps based exclusively on remotely sensed data which can be applied in any location, regardless of remoteness or accessibility. For this purpose, our approach allows forested terrain to be captured in the PRA model on a basic level and broadens the range of avalanche terrain that the model can be applied to.

4.4.2 Uncertainty in validation data

One of the key differences in relying on local expertise for model validation is the necessity to incorporate uncertainty. There are two distinct types of uncertainty that are relevant for validating the PRA model: 1) Uncertainty in the accuracy of the observations, recollection, and experience of our collaborating guides, and 2) Uncertainty in the reference datasets we provided them with to transfer their knowledge into spatial datasets and precision of polygon drawing.

In the case of guide observations, the primary sources of uncertainty in determining the location of avalanche release areas are the variability of avalanche conditions, how often the terrain is observed throughout the season, the guides recollection of avalanche events, and the potential for altered snowpack structure due to frequent guiding. These limitations are inherent to relying on human recollection as a source of validation data. However, our approach for capturing validation polygons from local experts accommodates these limitations by allowing for fuzzy boundaries in drawing polygons, collecting validation data from multiple guides independently, and intentionally minimizing the specificity that we ask the guides to label the release area proportions (0%, 25%, 50%, 75%, 100%).

The process for collecting validation data from our collaborating guides evolved through frequent back and forth discussions. When applying the validation polygons to select optimal input parameters for our study area we accounted for the nature of the data collection by placing more emphasis on the performance of 0% and 100% polygons, which have the highest level of certainty for the guides and are the most spatially explicit. We also preferred input parameters that resulted in a PRA model that is biased toward overestimating release areas in order to account for the potential that the guides have not witnessed all possible combinations of snowpack and weather conditions in our study area, despite their extensive experience.

An example of how the guides' experience can influence our validation data set can be seen in the right half of the 'Rendezvous' ski run, where there are many severely overestimated validation polygons (Figure 12, panel c). According to our DEM, the slope angles in this area are predominantly in the low to mid thirties, which are within the range observed for human triggered avalanches (Schweizer and Lütschg, 2001). However, the guiding operation frequently uses this piece of terrain and intentionally manages the snowpack using skier traffic to minimize the potential for weak layers to form and persist on the surface (e.g., surface hoar). Frequent guiding use and intentional maintenance of weak layers can create a modified snowpack structure (Haegeli and Atkins, 2016) and has the potential to impact the guides' perception of release area potential. In areas where the guide's experience is largely based on modified snowpack structures there is a high potential for the PRA model to overestimate avalanche release compared to the validation data set.

4.5 Limitations

The primary limitations of this research are side effects of our aim to minimize the cost of input data production and create a flexible workflow to apply and validate the PRA model in remote and data sparse regions. Using a DSM as input for a PRA model has not been thoroughly tested, and the inability to detect bare ground features within forest canopy likely causes

665   localized errors in the PRA model. Recently, a comparison of high-resolution DSM and DTM models for avalanche runout

666   modelling demonstrated some of the limitations of a DSM for dynamic avalanche simulation (Brožová et al., 2020). We were

667   unable to test the accuracy of the SPOT6 DSM compared to a DTM due to the lack of alternative high-resolution data in our

668   study area.

669   Relying exclusively on optical satellite imagery to account for forest avalanche interaction provides limited detail on

670   meaningful forest characteristics. Explicit modelling of stem density, gap size, or crown cover could improve the PRA model's

671   ability to capture forest avalanche interaction (Dash et al., 2016; Wallner et al., 2015). However, our focus is on minimizing

672   field data collection to create a workflow that is applicable in remote areas.

673   Finally, the experience of local experts is not an ideal source to generate validation data compared to long term observation

674   records. Observations from individual experts are prone to biases in their experience and potential for faulty recollection. We

675   attempted to minimize these effects on our dataset by collaborating closely with the guides to develop a system for recording

676   their observations that allows for uncertainty and is based on independent observations of multiple guides.

677   **5 Conclusions**

678   This research aimed to increase the range of application for existing high-resolution PRA modelling by developing a cost-

679   effective workflow for generating the required input datasets, expanding current PRA modelling methods to include avalanche

680   forest interaction, and to create a novel approach for validating the model based on the local expertise of avalanche practitioners

681   for data sparse regions. The research produced an updated version of the Bühler et al. (2018) PRA model which enables high-

682   resolution avalanche terrain modelling in a vastly greater proportion of mountainous terrain than previously possible. This is

683   thanks to the widespread availability of the necessary satellite remote sensing input data and local expertise required to validate

684   and optimize the PRA model input parameters. The updated model also allows for inclusion of forested terrain with varying

685   densities, contributing to a substantial improvement in the performance of the PRA model in our study area.

686   The data preparation pipeline developed for this research is based on open source software and intended to be reproducible in

687   areas without existing high-resolution DEM and forest cover data sets, which achieves our goal of making high-resolution

688   PRA modelling more accessible in remote and data sparse areas. Producing a satellite stereo DSM based on raw imagery

689   provides control over the DSM characteristics and minimizes the cost associated with acquiring this essential data set. Further

690   testing of the DSM pipeline developed for this research is required, especially in forested terrain, and could provide a

691   meaningful direction for future research.

692   Using locally optimized input parameters, our updated PRA model has a higher overall accuracy and less underestimated

693   release areas compared to the default parameters developed for Davos, Switzerland in Bühler et al. (2018). Our validation

694   approach utilizes local expertise to collect avalanche release area polygons via a custom-built online mapping tool and applies

695   spatial and statistical analysis to quantify the accuracy of the PRA model. We leveraged this unique validation data set to

696 develop a new polygon based grid search approach to optimize the PRA model input parameters. Creating a validation method
697 that allows for optimization of the PRA model in areas without a long standing avalanche observation dataset is essential to
698 evaluate the PRA model performance in new locations. This method also provides the opportunity for comparison of optimal
699 input parameters in different snow and avalanche climates. Future research applying the PRA model in maritime and
700 continental snow climates would provide additional insight into how the input parameters can be optimized for a broader range
701 of snowpack and avalanche conditions, which are not captured in the existing Davos or Galena study areas.

702 To include forested terrain in the PRA model we focused on creating a simple addition to the existing PRA model which does
703 not require any additional input data and remains an optional extension of the existing PRA model framework. We also focused
704 on maintaining the ability to create the input data sets via optical satellite remote sensing methods to minimize the overhead
705 cost and effort to produce forest characteristic data. Our approach allows the PRA model to capture the interactions between
706 forests and avalanche release by controlling the *forest density* where the PRA model is applied and altering the *slope angle*
707 *minimum* threshold based on the local forest density. These two changes are simple yet effective methods to account for forest
708 cover in PRA modelling.

709 Additional research focused on satellite imagery based modelling of forest characteristics (Dash et al., 2016; Hyyppä et al.,
710 2000; Rahimizadeh et al., 2020), such as stem density and gap size, could further improve the performance of PRA models in
711 forested terrain. While the availability of high-resolution LiDAR, laser scanning, or field measured forest characteristics are
712 essential for meaningfully validating the derivation of these datasets (Ginzler and Hobi, 2015; Waser et al., 2015), this type of
713 development and analysis was beyond the scope of this research. The forest regions in our study area are dominated by
714 coniferous tree species, which limits our ability to generalize the effectiveness of the PRA model in coniferous or mixed forest
715 ecosystems. Hence, we encourage other researchers to explore our approach in other forest types.

716 Despite the limitations and shortcomings of our approach, the present research improves the accessibility of high-resolution
717 PRA modelling by combining an existing state of the art PRA model with open source software tools and low cost input data
718 and presenting a flexible validation method to assess accuracy of the model output based on local terrain expertise. These
719 developments have the potential to enable a more widespread application of high-resolution avalanche terrain indication
720 modelling worldwide.

721 **Code and data availability.**

722 The data, code, and output for our analysis and the data and code for the figures and tables included in this paper are available
723 at osf.io/yq5s3 (Sykes et al., 2021).

Author contributions

JS created the data preprocessing workflow and input data sets with guidance from YB and PH. YB provided the original PRA model. JS developed the *forest density* and *forest slope scalar* modification to the PRA model. PH and JS collaborated with CMH Galena guides to collect validation data and implement online mapping tools to record the data. JS developed the validation and grid search methods with guidance from PH. JS prepared the manuscript with contributions from all co–authors.

Competing interests

YB and PH are members of the editorial board of Natural Hazards and Earth Science Sciences. The authors do not declare any other competing interests.

Acknowledgements

We wish to acknowledge our collaborators on this research from WSL Institute for Snow and Avalanche Research (SLF) and Canadian Mountain Holidays Galena Lodge. In particular, we would like to thank Roger Atkins and Mike Welch for their contribution to this work with their numerous conversations to develop our validation data collection methods and their time and effort in translating their experience into a validation data set. This research was enabled in part by the support and computer resources provided by WestGrid (www.westgrid.ca) and Compute Canada (www.computecanada.ca). The NSERC Industrial Research Chair in Avalanche Risk Management at Simon Fraser University is financially supported by Canadian Pacific Railway, HeliCat Canada, Mike Wiegele Helicopter Skiing and the Canadian Avalanche Association. The research program receives additional support from Avalanche Canada and the Avalanche Canada Foundation. The NSERC Industrial Research Chair in Avalanche Risk Management receives financial support from HeliCat Canada, the trade association of mechanized skiing operations in Canada.

Financial support

This research was funded by the Government of Canada Natural Sciences and Engineering Research Council via the NSERC Industrial Research Chair in Avalanche Risk Management at Simon Fraser University (grant no. IRC/515532-2016).

References

Andres, J. A. and Chueca Cía, J.: Mapping of avalanche start zones susceptibility: Arazas basin, Ordesa and Monte Perdido National Park (Spanish Pyrenees), J. Maps, 8, 14–21, https://doi.org/10.1080/17445647.2012.668414, 2012.

749 Barbolini, M., Pagliardi, M., Ferro, F., and Corradeghini, P.: Avalanche hazard mapping over large undocumented areas, Nat.
750 Hazards, 56, 451–464, https://doi.org/10.1007/s11069-009-9434-8, 2011.

751 Bebi, P., Kulakowski, D., and Rixen, C.: Snow avalanche disturbances in forest ecosystems - State of research and implications
752 for management, Forest Ecol. Manag., 257, 1883–1892, https://doi.org/10.1016/J.FORECO.2009.01.050, 2009.

753 Beyer, R. A., Alexandrov, O., and McMichael, S.: The Ames Stereo Pipeline: NASA's Open Source Software for Deriving
754 and Processing Terrain Data, Earth Sp. Sci., 5, 537–548, https://doi.org/10.1029/2018EA000409, 2018.

755 Boyd, J., Haegeli, P., Abu-Laban, R. B., Shuster, M., and Butt, J. C.: Patterns of death among avalanche fatalities: a 21-year
756 review., Can. Med. Assoc. J., 180, 507–12, https://doi.org/10.1503/cmaj.081327, 2009.

757 Brožová, N., Fischer, J. T., Bühler, Y., Bartelt, P., and Bebi, P.: Determining forest parameters for avalanche simulation using
758 remote sensing data, Cold Reg. Sci. Technol., 172, 102976, https://doi.org/10.1016/j.coldregions.2019.102976, 2020.

759 Bühler, Y., Hüni, A., Christen, M., Meister, R., and Kellenberger, T.: Automated detection and mapping of avalanche deposits
760 using airborne optical remote sensing data, Cold Reg. Sci. Technol., 57, 99–106,
761 https://doi.org/10.1016/j.coldregions.2009.02.007, 2009.

762 Bühler, Y., Kumar, S., Veitinger, J., Christen, M., and Stoffel, A.: Automated identification of potential snow avalanche release
763 areas based on digital elevation models, Nat. Hazard. Earth Sys., 13, 1321–1335, https://doi.org/10.5194/nhess-13-1321-2013,
764 2013.

765 Bühler, Y., Adams, M. S., Stoffel, A., and Boesch, R.: Photogrammetric reconstruction of homogenous snow surfaces in alpine
766 terrain applying near-infrared UAS imagery, Int. J. Remote Sens., 38, 3135–3158,
767 https://doi.org/10.1080/01431161.2016.1275060, 2017.

768 Bühler, Y., von Rickenbach, D., Christen, M., Margreth, S., Stoffel, L., Stoffel, A., and Kuhne, R.: Linking Modelled Potential
769 Release Areas with Avalanche Dynamic Simulations: An Automated Approach for Efficient Avalanche Hazard Indication
770 Mapping, in: Proceedings International Snow Science Workshop, 810–814, 2018.

771 Bühler, Y., von Rickenbach, D., Stoffel, A., Margreth, S., Stoffel, L., and Christen, M.: Automated snow avalanche release
772 area delineation - validation of existing algorithms and proposition of a new object-based approach for large-scale hazard
773 indication mapping, Nat. Hazard. Earth Sys., 18, 3235–3251, https://doi.org/10.5194/nhess-18-3235-2018, 2018.

774 Bühler, Y., Hafner, E. D., Zweifel, B., Zesiger, M., and Heisig, H.: Where are the avalanches? Rapid SPOT6 satellite data
775 acquisition to map an extreme avalanche period over the Swiss Alps, Cryosphere, 13, 3225–3238, https://doi.org/10.5194/tc-
776 13-3225-2019, 2019.

777 Casteller, A., Häfelfinger, T., Cortés Donoso, E., Podvin, K., Kulakowski, D., and Bebi, P.: Assessing the interaction between
778 mountain forests and snow avalanches at Nevados de Chillán, Chile and its implications for ecosystem-based disaster risk
779 reduction, Nat. Hazard. Earth Sys., 18, 1173–1186, https://doi.org/10.5194/nhess-18-1173-2018, 2018.

780 Christen, M., Kowalski, J., and Bartelt, P.: RAMMS: Numerical simulation of dense snow avalanches in three-dimensional
781 terrain, Cold Reg. Sci. Technol., 63, 1–14, https://doi.org/10.1016/j.coldregions.2010.04.005, 2010.

782   Chueca Cía, J., Andrés, A. J., and Montañés Magallón, A.: A proposal for avalanche susceptibility mapping in the Pyrenees
783   using GIS: the Formigal-Peyreget area (Sheet 145-I; scale 1:25.000), J. Maps, 10, 203–210,
784   https://doi.org/10.1080/17445647.2013.870501, 2014.

785   Colorado Avalanche Information Center (CAIC), [online] Available from: https://avalanche.state.co.us/accidents/statistics-
786   and-reporting/, last access: 27 April 2020.

787   Dash, J. P., Watt, M. S., Bhandari, S., and Watt, P.: Characterising forest structure using combinations of airborne laser
788   scanning data, RapidEye satellite imagery and environmental variables, Forestry, 89, 159–169,
789   https://doi.org/10.1093/forestry/cpv048, 2016.

790   Facciolo, G., De Franchis, C., and Meinhardt, E.: MGM: A Significantly More Global Matching for Stereovision, 2015.

791   Feistl, T., Bebi, P., Teich, M., Bühler, Y., Christen, M., Thuro, K., and Bartelt, P.: Observations and modeling of the braking
792   effect of forests on small and medium avalanches, 60, 124–138, https://doi.org/10.3189/2014JoG13J055, 2014.

793   Feistl, T., Bebi, P., Christen, M., Margreth, S., Diefenbach, L., and Bartelt, P.: Forest damage and snow avalanche flow regime,
794   Nat. Hazard. Earth Sys., 15, 1275–1288, https://doi.org/10.5194/nhess-15-1275-2015, 2015.

795   GDAL Contributors,: GDAL/OGR Geospatial Data Abstraction software Library., 2021.

796   Ghinoi, A. and Chung, C.-J.: STARTER: a statistical GIS-based model for the prediction of snow avalanche susceptibility
797   using terrain features-application to Alta Val Badia, Italian Dolomites, Geomorphology, 66, 305–325,
798   https://doi.org/10.1016/j.geomorph.2004.09.018, 2005.

799   Gillies, S. and Others: Rasterio: geospatial raster I/O for Python programmers, https://github.com/mapbox/rasterio, 2013.

800   Ginzler, C. and Hobi, M.: Countrywide Stereo-Image Matching for Updating Digital Surface Models in the Framework of the
801   Swiss National Forest Inventory, Remote Sens-Basel, 7, 4343–4370, https://doi.org/10.3390/rs70404343, 2015.

802   Gruber, U. and Haefner, H.: Avalanche hazard mapping with satellite data and a digital elevation model, Appl. Geogr., 15,
803   99–113, https://doi.org/10.1016/0143-6228(94)00004-A, 1995.

804   Haegeli, P. and Atkins, R.: Managing the Physical Risk From Avalanches in a Helicopter Skiing Operation--Merging and
805   Contrasting Gps Tracking Data with the Operational Guiding Perspective, in: Proceedings International Snow Science
806   Workshop, 104–111, 2016.

807   Haegeli, P. and McClung, D. M.: Expanding the snow-climate classification with avalanche-relevant information: initial
808   description of avalanche winter regimes for southwestern Canada, J. Glaciol., 53, 266–276,
809   https://doi.org/10.3189/172756507782202801, 2007.

810   Hafner, E. D., Techel, F., Leinss, S., and Bühler, Y.: Mapping avalanches with satellites – evaluation of performance and
811   completeness, Cryosphere, 15, 983–1004, https://doi.org/10.5194/tc-15-983-2021, 2021.

812   Hägeli, P. and McClung, D. M.: Avalanche characteristics of a transitional snow climate—Columbia Mountains, British
813   Columbia, Canada, Cold Reg. Sci. Technol., 37, 255–276, https://doi.org/10.1016/S0165-232X(03)00069-7, 2003.

814 Harris, C. R., Millman, K. J., van der Walt, S. J., Gommers, R., Virtanen, P., Cournapeau, D., Wieser, E., Taylor, J., Berg, S.,
815 Smith, N. J., Kern, R., Picus, M., Hoyer, S., van Kerkwijk, M. H., Brett, M., Haldane, A., del Río, J. F., Wiebe, M., Peterson,
816 P., Gérard-Marchant, P., Sheppard, K., Reddy, T., Weckesser, W., Abbasi, H., Gohlke, C., and Oliphant, T. E.: Array
817 programming with NumPy, Nature, 585, 357–362, https://doi.org/10.1038/s41586-020-2649-2, 2020.

818 Harvey, S., Schmudlach, G., Buhler, Y., Durr, L., Stoffel, A., and Christen, M.: Avalanche Terrain Maps for Backcountry
819 Skiing in Switzerland, in: Proceedings International Snow Science Workshop, 300, 2018.

820 Höhle, J. and Höhle, M.: Accuracy assessment of digital elevation models by means of robust statistical methods, ISPRS J.
821 Photogramm., 64, 398–406, https://doi.org/10.1016/j.isprsjprs.2009.02.003, 2009.

822 Hyyppä, J., Hyyppä, H., Inkinen, M., Engdahl, M., Linko, S., and Zhu, Y. H.: Accuracy comparison of various remote sensing
823 data sources in the retrieval of forest stand attributes, Forest Ecol. Manag., 128, 109–120, https://doi.org/10.1016/S0378-
824 1127(99)00278-9, 2000.

825 Jamieson, Bruce., Haegeli, P., and Gauthier, D.: Avalanche accidents in Canada, Canadian Avalanche Association, 2010.

826 Korzeniowska, K., Bühler, Y., Marty, M., and Korup, O.: Regional snow-avalanche detection using object-based image
827 analysis of near-infrared aerial imagery, Nat. Hazard. Earth Sys., 17, 1823–1836, https://doi.org/10.5194/nhess-17-1823-2017,
828 2017.

829 Kramm, T. and Hoffmeister, D.: EVALUATION OF DIGITAL ELEVATION MODELS FOR GEOMORPHOMETRIC
830 ANALYSES ON DIFFERENT SCALES FOR NORTHERN CHILE, Int. Arch. Photogramm. Remote Sens. Spat. Inf. Sci.,
831 XLII-2/W13, 1229–1235, https://doi.org/10.5194/isprs-archives-XLII-2-W13-1229-2019, 2019.

832 Kuhn, M. and Johnson, K.: Applied predictive modeling, 1–600 pp., https://doi.org/10.1007/978-1-4614-6849-3, 2013.

833 Kumar, S., Srivastava, P. K., Gore, A., and Singh, M. K.: Fuzzy-frequency ratio model for avalanche susceptibility mapping,
834 Int. J. Digit. Earth, 9, 1168–1184, https://doi.org/10.1080/17538947.2016.1197328, 2016.

835 Kumar, S., Srivastava, P. K., Snehmani, and Bhatiya, S.: Geospatial probabilistic modelling for release area mapping of snow
836 avalanches, Cold Reg. Sci. Technol., 165, 102813, https://doi.org/10.1016/J.COLDREGIONS.2019.102813, 2019.

837 Lato, M. J., Frauenfelder, R., and Bühler, Y.: Automated detection of snow avalanche deposits: segmentation and classification
838 of optical remote sensing imagery, Nat. Hazard. Earth Sys., 12, 2893–2906, https://doi.org/10.5194/nhess-12-2893-2012,
839 2012.

840 Lutz, E. R. and Birkeland, K. W.: Spatial patterns of surface hoar properties and incoming radiation on an inclined forest
841 opening, J. Glaciol., 57, 355–366, https://doi.org/10.3189/002214311796405843, 2011.

842 Maggioni, M. and Gruber, U.: The influence of topographic parameters on avalanche release dimension and frequency, Cold
843 Reg. Sci. Technol., 37, 407–419, https://doi.org/10.1016/S0165-232X(03)00080-6, 2003.

844 Margreth, S. and Funk, M.: Hazard mapping for ice and combined snow/ice avalanches — two case studies from the Swiss
845 and Italian Alps, Cold Reg. Sci. Technol., 30, 159–173, https://doi.org/10.1016/S0165-232X(99)00027-0, 1999.

846 McClung, D. and Schaerer, P.: The avalanche handbook, Mountaineers Books, 342 pp., 2006.

847 McClung, D. M.: Characteristics of terrain, snow supply and forest cover for avalanche initiation caused by logging, Ann.
848 Glaciol., 32, 223–229, https://doi.org/10.3189/172756401781819391, 2001.

849 Pedregosa, F., Varoquaux, G., Gramfort, A., Michel, V., Thirion, B., Grisel, O., Blondel, M., Prettenhofer, P., Weiss, R.,
850 Dubourg, V., Vanderplas, J., Passos, A., Cournapeau, D., Brucher, M., Perrot, M., and Édouard, D.: Scikit-learn: Machine
851 Learning in Python, J. Mach. Learn. Res., 2825–2830 pp., 2011.

852 Planet Team.: Planet Application Program Interface: In Space for Life on Earth, https://api.planet.com, 2017.

853 Pistocchi, A. and Notarnicola, C.: Data-driven mapping of avalanche release areas: a case study in South Tyrol, Italy, Nat.
854 Hazards, 65, 1313–1330, https://doi.org/10.1007/s11069-012-0410-3, 2013.

855 QGIS Development Team.: QGIS Geographic Information System, http://qgis.org, 2021.

856 Rahimizadeh, N., Babaie Kafaky, S., Sahebi, M. R., and Mataji, A.: Forest structure parameter extraction using SPOT-7
857 satellite data by object- and pixel-based classification methods, Environ. Monit. Assess., 192, 43,
858 https://doi.org/10.1007/s10661-019-8015-x, 2020.

859 Rudolf-Miklau, F., Skolaut, C., and Sauermoser, S.: Avalanche Hazard Assessment and Planning of Protection Measures, in:
860 The Technical Avalanche Protection Handbook, 91–126, https://doi.org/10.1002/9783433603840.ch04, 2015.

861 Schweizer, J. and Lütschg, M.: Characteristics of human-triggered avalanches, Cold Reg. Sci. Technol., 33, 147–162, 2001.

862 Schneebeli, M. and Bebi, P.: Snow and Avalanche Control, Encycl. For. Sci., 397–402, 2004.

863 Shandro, B. and Haegeli, P.: Characterizing the nature and variability of avalanche hazard in western Canada, Nat. Hazard.
864 Earth Sys., 18, 1141–1158, https://doi.org/10.5194/nhess-18-1141-2018, 2018.

865 Sharp, E., Haegeli, P., and Welch, M.: Patterns in the exposure of ski guides to avalanche terrain, in: Proceedings International
866 Snow Science Workshop, 2018.

867 Shean, D. E., Alexandrov, O., Moratto, Z. M., Smith, B. E., Joughin, I. R., Porter, C., and Morin, P.: An automated, open-
868 source pipeline for mass production of digital elevation models (DEMs) from very-high-resolution commercial stereo satellite
869 imagery, ISPRS J. Photogramm., 116, 101–117, https://doi.org/10.1016/j.isprsjprs.2016.03.012, 2016.

870 Sykes, J., Haegeli, P., and Bühler, Y.: Automated snow avalanche release areas delineation in data sparse, remote, and forested
871 regions -- Code and Data, https://doi.org/10.17605/OSF.IO/YQ5S3, 2021.

872 Techel, F., Jarry, F., Kronthaler, G., Mitterer, S., Nairz, P., Pavšek, M., Valt, M., and Darms, G.: Avalanche fatalities in the
873 European Alps: long-term trends and statistics, Geogr. Helv., 71, 147–159, https://doi.org/10.5194/gh-71-147-2016, 2016.

874 Teich, M., Bartelt, P., Grêt-Regamey, A., and Bebi, P.: Snow Avalanches in Forested Terrain: Influence of Forest Parameters,
875 Topography, and Avalanche Characteristics on Runout Distance, Arct. Antarct. Alp. Res., 44, 509–519,
876 https://doi.org/10.1657/1938-4246-44.4.509, 2012.

877 Veitinger, J., Purves, R. S., and Sovilla, B.: Potential slab avalanche release area identification from estimated winter terrain:
878 a multi-scale, fuzzy logic approach, Nat. Hazard. Earth Sys., 16, 2211–2225, https://doi.org/10.5194/nhess-16-2211-2016,
879 2016.

880   Voellmy, A.: Über die Zerstörungskraft von Lawinen, Schweizerische Bauzeitung, 73, 159–165, 1955.

881   Wallner, A., Elatawneh, A., Schneider, T., and Knoke, T.: Estimation of forest structural information using RapidEye satellite

882   data, Forestry, 88, 96–107, https://doi.org/10.1093/forestry/cpu032, 2015.

883   Waser, L., Fischer, C., Wang, Z., Ginzler, C., Waser, L. T., Fischer, C., Wang, Z., and Ginzler, C.: Wall-to-Wall Forest

884   Mapping Based on Digital Surface Models from Image-Based Point Clouds and a NFI Forest Definition, Forests, 6, 4510–

885   4528, https://doi.org/10.3390/f6124386, 2015.